

Development of Neutron Monitor for Fusion Systems

by

Zhe Li

A thesis submitted to the
School of Graduate and Postdoctoral Studies in partial
fulfillment of the requirements for the degree of

Master of Applied Science in Nuclear Engineering

Faculty of Energy Systems and Nuclear Science

University of Ontario Institute of Technology (Ontario Tech University)

Oshawa, Ontario, Canada

April 2022

© Zhe Li, 2022

THESIS EXAMINATION INFORMATION

Submitted by: **Zhe Li**

Master of Applied Science in Nuclear Engineering

Thesis title:	Development of Neutron Monitor for Fusion Systems
---------------	---

An oral defense of this thesis took place on April 11, 2022 in front of the following examining committee:

Examining Committee:

Chair of Examining Committee	Dr. Jennifer McKellar
Research Supervisor	Dr. Rachid Machrafi
Examining Committee Member	Dr. Igor Pioro
Examining Committee Member	Dr. Kirk Atkinson
Thesis Examiner	Dr. Anthony Waker, University Examiner

The above committee determined that the thesis is acceptable in form and content and that a satisfactory knowledge of the field covered by the thesis was demonstrated by the candidate during an oral examination. A signed copy of the Certificate of Approval is available from the School of Graduate and Postdoctoral Studies.

ABSTRACT

Currently, the detection of neutrons employs sensors with a high thermal neutron response embedded in a thermalizing medium. However, this approach does not provide much information on neutron energy and, therefore, is inherently unable to identify sources commonly used in the industry. The current study proposes the use of a bi-atomic scintillator crystal, LaCl_3 , to detect fast neutrons above 1 MeV in general and develop a neutron monitor for (D, D) fusion reaction in particular. The approach uses the (n, p) reaction on a bi-atomic scintillator in the neutron energy range above 1 MeV. Thus, a series of Monte Carlo simulations have been performed using MCNP/X along with a series of experiments carried out using a neutron generator based on the (D, D) reaction at 10^6 n/s. Both sets of data were compared in term of the pulse height spectra. The analysis of the data suggests that a prominent peak from the emitted protons can serve to monitor the neutron emission from the generator.

Keywords: neutron; neutron spectra; lanthanum chloride; radiation detection; neutron generator

AUTHOR'S DECLARATION

I hereby declare that this thesis consists of original work of which I have authored. This is a true copy of the thesis, including any required final revisions, as accepted by my examiners.

I authorize the University of Ontario Institute of Technology (Ontario Tech University) to lend this thesis to other institutions or individuals for the purpose of scholarly research. I further authorize University of Ontario Institute of Technology (Ontario Tech University) to reproduce this thesis by photocopying or by other means, in total or in part, at the request of other institutions or individuals for the purpose of scholarly research. I understand that my thesis will be made electronically available to the public.

Zhe Li

ZHE LI

STATEMENT OF CONTRIBUTIONS

The experiment described in Chapter 3 was performed at the Ontario Tech University in Oshawa, Ontario, using the neutron facility operated by Faculty of Energy Systems and Nuclear Science. My duties involved setting up the experiment and using the neutron generator to collect results.

Part of the work described in Chapter 1 and Chapter 3 has been published as:

Z. Li¹, R. Machrafi², E.A Tamimi³, C. Nayve⁴ (2021). “Development of Neutron Monitor for Fusion System”. 40th Annual Conference of the Canadian Nuclear Society and 45th Annual CNS/CNA Student Conference.

I performed the majority of the experiment, and writing of the paper.

ACKNOWLEDGEMENT

I would like to thank Dr. Rachid Machrafi for his guidance on my master research, as well as all the knowledge and support since 2016.

I also like to thank Dr. Igor Pioro for his support my master study and job applications.

My gratitude extends to Jarret Burgener and Isaac Lee for their continuous support of my thesis paper.

Lastly, my thanks also goes to our faculty, FESNS, provides such a great environment for me to develop here for 7 years.

TABLE OF CONTENTS

THESIS EXAMINATION INFORMATION.....	ii
ABSTRACT.....	iii
AUTHOR’S DECLARATION.....	iv
STATEMENT OF CONTRIBUTIONS	v
ACKNOWLEDGEMENT	vi
TABLE OF CONTENTS.....	vii
LIST OF FIGURES	xi
LIST OF TABLES	xiii
LIST OF ABBREVIATIONS AND SYMBOLS	xiv
Greek Symbols.....	xvii
Subscripts.....	xviii
Chapter 1: INTRODUCTION.....	1
1.1 Objective of the Thesis	3
1.2 References.....	5
Chapter 2: NEUTRON INTERACTION AND DETECTION.....	7
2.1 Neutron Sources.....	7
2.1.1 Spontaneous Fission.....	7
2.1.2 Radioisotope Based Source (α , n) Reactions	9
2.1.3 Photoneutron Sources (γ , n) Reaction.....	10

2.1.4 Fusion Sources	12
2.2 Neutron Interaction	14
2.2.1 Elastic Scattering	15
2.2.2 Inelastic Scattering	16
2.2.3 Radiative Capture.....	17
2.2.4 Transmutation (n, x) Reaction	17
2.2.5 Fission Reaction.....	18
2.3 Neutron Cross-section.....	19
2.4 Neutron Detector Properties	23
2.4.1 Neutron Detector Mechanisms	23
2.4.2 Detector Operation Modes	24
2.4.3 Energy Resolution.....	24
2.4.4 Detection Efficiency	25
2.4.5 Dead Time.....	27
2.5 Common Neutron Detectors	30
2.5.1 Slow Neutron Detection.....	30
2.5.2 Fast Neutron Detection	34
2.5.2 (a) Neutron Moderation Type Detector	34
2.5.2 (b) Neutron Scattering Detectors	36
2.5.2 (c) Fast Neutron Reaction Based Proportional Detectors	37

2.6 References.....	39
Chapter 3: METHODOLOGY DESCRIPTION.....	41
3.1 ³⁵ Cl Nuclear Reactions.....	41
3.1.1 ³⁵ Cl (n, p) ³⁵ S Reaction	42
3.1.2 ³⁵ Cl(n, α) ³² P Reaction	44
3.2 Monte Carlo Simulation.....	46
3.2.1 MCNP Model.....	46
3.3 Experimental Apparatus.....	48
3.3.1 LaCl ₃ Scintillator Description.....	48
3.3.2 Electronic and Software.....	50
3.3.3 Laboratory Description	52
3.3.4 Neutron Generator	54
3.4 Experimental Procedure.....	55
3.4.1 Background and calibration adjustment.....	56
3.4.2 Neutron Detection Procedure.....	56
3.5 References.....	58
Chapter 4: RESULTS AND DISCUSSION	59
4.1 Background and Detector Calibration	59
4.1.1 Background Measurement	59
4.1.2 Detector Calibration.....	60

4.2 Gamma Detection and Detector Resolution	63
4.3 MCNP Simulation Results	68
4.4 Experimental Results	74
4.5 Comparison	76
Chapter 5: CONCLUSION	77
Chapter 6: FUTURE WORK	79
BIBLIOGRAPHY	80
APPENDIXES	86
Appendix A – Materials Tables in MCNP/X	86
A.1 sub-Appendix	87
Appendix B – MCNP/X Code for ^{22}Na Gamma Detection	88
Appendix C – MCNP/X Code for ^{35}Cl (n, p) ^{35}S Reaction	89
Appendix D – MCNP/X Code for ^{35}Cl (n, α) ^{32}P Reaction	91
Appendix E – MCNP/X Code for ^{35}Cl (n, γ) Reaction	93

LIST OF FIGURES

CHAPTER 2

Figure 2.1: ^{252}Cf Decay scheme with probabilities [16].	8
Figure 2.2: D-D and D-T neutron generation [19].	12
Figure 2.3: Neutron elastic scattering schematic and reaction.	15
Figure 2.4: Neutron inelastic scattering schematic and reaction.	16
Figure 2.6: Neutron Radiative Capture Schematic and Reaction.	17
Figure 2.7: Fission cross-section of U-235 and Pu-239 [25].	19
Figure 2.8: Two dead time models[26].	27
Figure 2.9: Gas filled proportional counter schematic [30].	32
Figure 2.10: BF_3 gas filled proportional counter spectrum[31].	33
Figure 2.11: Spherical detector schematic[33].	35
Figure 2.12: Fast neutron cross-section of the $^3\text{He}(n, p)$ reaction [34].	37

CHAPTER 3

Figure 3.1: Nuclear reaction energy of ^{36}Cl , ^{35}S , and ^{32}P [35].	41
Figure 3.2: Illustration of a $^{35}\text{Cl}(n, p)^{35}\text{S}$ reaction.	42
Figure 3.3: $^{35}\text{Cl}(n, p)^{35}\text{S}$ reaction cross-section [36].	43
Figure 3.4: Illustration of a $^{35}\text{Cl}(n, \alpha)^{32}\text{P}$ reaction.	44
Figure 3.5: Cross-section of $^{35}\text{Cl}(n, p)^{35}\text{S}$ reaction and $^{35}\text{Cl}(n, \alpha)^{32}\text{P}$ reaction [36].	45
Figure 3.6: MCNP model of the LaCl_3 detector.	47
Figure 3.7: $\text{LaCl}_3:\text{Ce}$ scintillator crystal[38].	49
Figure 3.8: Detector schematic.	50
Figure 3.9: Gamma Acquisition & Analysis and OriginPro 9.1 interface [39].	51

Figure 3.10: Experimental setup for neutron detection.	53
---	----

CHAPTER 4

Figure 4.1: Background spectra.	59
Figure 4.2: Calibration line of the detector with ^{137}Cs and ^{22}Na	61
Figure 4.3: Calibrated response function of the $\text{LaCl}_3:\text{Ce}$ scintillator using ^{137}Cs and ^{22}Na gamma sources.....	62
Figure 4.4: Measured pulse height spectrum of LaCl_3 using ^{22}Na gamma source.	63
Figure 4.5: Pulse height spectrum of LaCl_3 using ^{22}Na gamma source.....	66
Figure 4.6: $^{35}\text{Cl}(\text{n}, \text{p})$ response function of the LaCl_3 detector to 2.5 MeV neutrons with only protons tallied.....	68
Figure 4.7: $^{35}\text{Cl}(\text{n}, \alpha)$ response function of the LaCl_3 detector to 2.5 MeV neutrons with only alpha particles tallied.	70
Figure 4.8: $^{35}\text{Cl}(\text{n}, \alpha)$ and $^{35}\text{Cl}(\text{n}, \text{p})$ response function of the LaCl_3 detector to 2.5 MeV neutrons with protons and alpha particles tallied together.	71
Figure 4.9: $^{35}\text{Cl}(\text{n}, \alpha)$ and $^{35}\text{Cl}(\text{n}, \text{p})$ response function of the LaCl_3 detector to 2.5 MeV neutrons with only gammas tallied.	72
Figure 4.10: $^{35}\text{Cl}(\text{n}, \alpha)$ and $^{35}\text{Cl}(\text{n}, \text{p})$ response function of the LaCl_3 detector to 2.5 MeV neutrons with protons, gammas, and alpha particles tallied.	73
Figure 4.11: Measured response function of the $\text{LaCl}_3:\text{Ce}$ scintillator with 2.5 MeV neutrons...	74
Figure 4.12: Comparison of measured response functions for each run.....	75
Figure 4.13: Comparison of the simulated and measured response function of LaCl_3 with 2.5 MeV	76

LIST OF TABLES

CHAPTER 2

Table 2.1: Characteristics of Be (α , n) neutron sources[15]	9
Table 2.2: Neutron interaction methods.....	14
Table 2.3: Properties of $^{10}\text{B}(n, \alpha)$, $^6\text{Li}(n, \alpha)$, and $^3\text{He}(n, p)$ reactions. (Data from [28])	31

CHAPTER 3

Table 3.1: Experimental setup information for the seven measurements.	55
--	----

CHAPTER 4

Table 4.1: Calibration data of detector with ^{137}Cs and ^{22}Na from measured data.	60
Table 4.2: Coordinates for FWHM calculations and FWHM values.	65

APPENDIXES A

Table A.0.1: Material Input for Lathanum Choride.....	86
Table A.0.2: Material Input for Air	86
Table A.0.3: Material Input for Heavy Concrete[40]	86

LIST OF ABBREVIATIONS AND SYMBOLS

A	Atomic Weight, amu
Am	Americium
Be	Beryllium
Cf	Californium
Cl	Chloride
Cm	Curium
d	Thickness, cm
D	Deuterium
eV	Electron Volt
eeV	Equivalent Electron Volt
E_n	Neutron Energy
E_p	Proton Energy
E_{peak}	Energy of the Peak
E_R	Recoil Nucleus Energy
E_γ	Gamma Energy

<i>ERC</i>	Energy Research Center
<i>FWHM</i>	Full Width at Half Maximum
<i>GEB</i>	Gaussian Energy Broadening
<i>H₀</i>	Channel# of the Pulse Height
<i>He</i>	Helium
<i>HFIR</i>	High Flux Isotopes Reactor
<i>HV</i>	High Voltage
<i>I</i>	Attenuated Intensity, neutrons * s ⁻¹
<i>I₀</i>	Initial Intensity, neutrons * s ⁻¹
<i>La</i>	Lanthanum
<i>m</i>	Recorded Count Rate
<i>MCA</i>	Multichannel Analyzer
<i>MCNP</i>	Monte Carlo N-Particle Transport Code
<i>MeV/c²</i>	Mass unit, c = 2.99792*10 ⁸ m/s
<i>MSV</i>	Mean Square Voltage
<i>n</i>	True Interaction Rate

<i>N</i>	Atomic Density, cm^{-3}
<i>N_A</i>	Avogadro Number, $1.023 \times 10^{23} \text{ mol}^{-1}$
<i>PC</i>	Personal Computer
<i>PMT</i>	Photomultiplier Tube
<i>Po</i>	Polonium
<i>Pu</i>	Plutonium
<i>Q</i>	Reaction Quotient Value
<i>r</i>	Distance, cm
<i>R</i>	Reaction Rate, number of interactions * $\text{cm}^{-3} \cdot \text{s}^{-1}$, or Peak Resolution.
<i>Ra</i>	Radium
<i>S</i>	Sulfur
<i>T</i>	Tritium
<i>T_{1/2}</i>	Half-life

Greek Symbols

α	Alpha particles
γ	Gamma-rays
ρ	Material Density, g*cm ⁻³
σ	Microscopic Cross-section, barn or cm ² (1 barn = 10 ⁻²⁴ cm ²)
Σ	Macroscopic Cross-section, cm ⁻¹
θ	Angle
φ	Neutron Flux, neutrons* cm ⁻² * s ⁻¹
ε_{abs}	Absolute Efficiency
ε_{int}	Intrinsic Efficiency
ε_{ip}	Peak Efficiency
τ	System Dead Time
Ω	Solid Angle of the Detector from the Source Position

Subscripts

n	Neutron
p	Proton
f	Fragment

CHAPTER 1: INTRODUCTION

The discovery of the neutron goes back to 1932, almost forty years after the first X-rays was discovered by Wilhelm Conrad Röntgen. In those forty years, scientists discovered most of the particles within the atomic model, however, there were still unable to explain the reason why the positively charged particles, protons, could be held together with their strong repulsive forces in the nuclei, as well as the mass number and the atomic number not matching with each other [1]. In 1932, this problem was solved by James Chadwick, who discovered the neutron and explained the difference between the atomic number and mass number as well as proved that the neutron has a nuclear force that has the ability to hold the protons together in the nuclei[1]. The discovery of neutron not only proved the theory that isotopes exists by Soddy in 1913, but also contributed to the discovery of other fundamental particles [1].

The neutron (n) is a subatomic uncharged particle, its mass is $939.565 \text{ MeV}/c^2$, which is slightly heavier than a proton (p). Unlike the other charged particles (such as proton, electron, and positron) or radiation (such as gamma radiation) that lose their energy while penetrating materials, the neutron does not interact through Coulomb forces. It can travel through several centimeters of material without interacting with other particles, as well as remain undetected during this process since there is no charge [2]. Once the neutron finally reaches the point where it is interacting with the nuclei of the absorbing material, it can either be captured, or it undergoes scattering [2]. When the neutron is captured, secondary radiation such as gamma rays and fast electrons can be produced. Furthermore, if the neutron interacts with an absorber nucleus, heavy particles such as recoiled protons and fission fragments can be observed [2]. For radiation detection, all types of detectors are measuring the interaction between the incident radiation and the material of the detector. This interaction can be measured using either the primary radiation or the secondary radiation emitted.

Due to the fact that neutrons are uncharged, they cannot cause ionization or excitation of the detection medium, which makes it very difficult to detect neutron directly. Therefore, neutrons can only be detected by measuring the energy of the secondary radiations emitted after neutron interaction.

Most existing technology for fast neutron detection uses sensors with a high thermal neutron response material such as helium, lithium, and boron enclosed in a thermalizing medium. Due to reasonable detection efficiency and good discrimination ability against gamma rays this approach has been used for decades. However, it provides no information on neutron energy, therefore, it is unable to identify neutron sources commonly encountered in various neutron fields. Furthermore, this technology is unable to quantitatively evaluate the output of neutron sources. The second approach for fast neutron detection uses the neutron scattering process on hydrogen, usually in the form of plastic or liquid scintillators. With this method, the neutron energy transferred to the scattered proton highly depends on the scattered angle, and consequently, a continuous distribution of energies from the scattered protons is observed on pulsed-height spectra. Thus, to determine the incident neutron energy spectra, complicated unfolding techniques are required. In addition, these detectors have a lower light output for neutrons when compared to gamma rays, therefore, they cannot be distinguished from a gamma-ray signal. This is another major problem with neutron spectrometry in mixed fields.

The above-mentioned limitations demonstrate the importance of two key points in neutron spectrometry; the physical properties of the neutron sensor, and the algorithms involved in the spectrum unfolding. For the neutron sensor's physical properties, limitations are mainly related to the detection efficiency and the energy dependence, both of which are associated with the basic physical properties of the neutron sensor [3-6]. Recently, there have been newly developed sensors

based on multi-elements to produce high detection efficiency scintillators. Among them, the $\text{Cs}_2\text{LiYCl}_6\text{:Ce}$ (CLYC) family has been tested for thermal as well as for fast neutrons [7-12]. However, besides the ^6Li isotope, the sensor also contains ^{35}Cl , in which a useful reaction can be utilized for fast neutron detection i.e., $^{35}\text{Cl} (n, p) ^{35}\text{S}$. This reaction has been studied in one of our previous works for low energy neutrons and recently with thermal and 2.5 MeV neutrons[13]. The cross-section of this reaction for energies greater than a few hundred keV can play a significant role in fast neutron spectrometry for neutron identification, therefore, one may overcome the challenge that traditionally faced neutron detectors. In the previous paper [14], there has not been seen any sign of protons emitted in the $^{35}\text{Cl} (n, p) ^{35}\text{S}$ reaction when a ^6Li -enriched CLYC has been exposed to fast neutrons due to the dominance of the $^6\text{Li} (n, \alpha) ^3\text{H}$ reaction. Instead, a new version of the CLYC referred to as ^7Li -enriched CLYC (99% ^7Li enriched) has been used. However, in the current study, it is proposed to eliminate the use of the crystal composed of the ^6Li isotope and investigate the same reaction using a crystal composed of LaCl_3 instead.

1.1 Objective of the Thesis

The objective of this thesis intends to study the response function of the LaCl_3 scintillator and use it as a monitor for fast neutrons produced in fusion systems. It focuses on analyzing the results of a series of experiments to investigate the capability of the LaCl_3 scintillator to detect fast neutrons along with a series of Monte Carlo simulations to identify different features observed on the pulse height spectra using a (D, D) neutron generator. Both neutron and gamma pulse height spectra were measured and analyzed.

The thesis consists of an introduction, three chapters, a conclusion, future work, references lists, and appendixes. The introduction section gives a brief overview of the discovery of neutrons,

neutrons properties, and current neutron detection techniques. The objective of this thesis is also provided at the end of the introduction.

Chapter one presents s a literature review on neutron background, which includes information on various, neutron sources, neutron interactions, cross-sections, and the current techniques used for neutron detection. Chapter two describes the methodology of the thesis; which includes the neutron reactions with ^{35}Cl , MCNP/X simulations, and the experiment setup. Chapter 3 presents the results of the measurements and simulations along with a discussion and analysis. Finally, the thesis concludes with the main findings and ends with a reference list and appendixes.

1.2 References

1. Magill, J. and J. Galy, *1. Origins and Discovery: The Neutron*, in *Radioactivity Radionuclides Radiation*. 2005, Springer: Berlin. p. 11-12.
2. Machrafi, R., *Neutron Interaction with Matter*. 2018, Ontario Tech University: Oshawa.
3. Alberts, W.G., et al., *Development of electronic personal neutron dosimeters: a European cooperation* *Radiation Protection Dosimetry*, 2001. **96**(1-3): p. 251-254.
4. Schutz, R., et al., *A Three Si Detector System For Personnel Neutron Dosimetry Developed By Means Of Monte Carlo Simulation Calculations*. *Radiation Protection Dosimetry*, 2003. **104**(1): p. 17-26.
5. Barthe, J., J.M. Bordy, and T. Lahaye, *Electronic Neutron Dosimeters: History and State of the Art*. *Radiation Protection Dosimetry*, 1997. **70**(1-4): p. 59-66.
6. Bartlett, D.T., R.J. Tanner, and D.J. Thomas, *Active Neutron Personal Dosimeters – A Review of Current Status*. *Radiation Protection Dosimetry*, 1999. **86**(2): p. 107-122.
7. Combes, C.M., et al., *Optical and scintillation properties of pure and Ce³⁺-doped Cs₂LiYCl₆ and Li₃YCl₆:Ce³⁺ crystals*. *Journal of Luminescence*, 1999. **82**(4): p. 299-305.
8. Bessiere, A., et al., *New thermal neutron scintillators: Cs₂/LiYCl₆:Ce³⁺ and Cs₂/LiYBr₆:Ce³⁺*. *IEEE Transactions on Nuclear Science*, 2004. **51**(5): p. 2970-2972.
9. Bessiere, A., et al., *Luminescence and scintillation properties of CS₂LiYCl₆:Ce³⁺ for γ and neutron detection*. *Nuclear Instruments and Methods in Physics Research Section A: Accelerators, Spectrometers, Detectors and Associated Equipment*, 2005. **537**(1-2): p. 242-246.

10. Glodo, J., et al., *Scintillation Properties of 1 Inch Cs₂LiYCl₆:Ce Crystals*. IEEE Transactions on Nuclear Science, 2008. **55**(3): p. 1206-1209.
11. Higgins, W.M., et al., *Bridgman growth of Cs₂LiYCl₆:Ce and ⁶Li-enriched Cs₂₆LiYCl₆:Ce crystals for high resolution gamma ray and neutron spectrometers*. Journal of Crystal Growth, 2010. **312**(8): p. 1216-1220.
12. Glodo, J., et al., *Selected Properties of Cs₂LiYCl₆, Cs₂LiLaCl₆, and Cs₂LiLaBr₆ Scintillators*. IEEE Transactions on Nuclear Science, 2011. **58**(1): p. 333-338.
13. Machrafi, R., A.L. Miller, and K. N., *New approach to neutron spectrometry with multi element scintillator*. Radiation Measurement, 2015. **80**(ELSEVIR Ltd.): p. 10-16.
14. Khan, N., *A New Approach to Neutron Spectrometry with Multi-Element Scintillators*. 2014, Ontario Tech University: Oshawa.

CHAPTER 2: NEUTRON INTERACTION AND DETECTION

2.1 Neutron Sources

Neutrons are located within the nucleus of an element. There are no natural neutron emitters, unlike gamma-ray sources, which have the ability to produce gamma radiation from different nuclei through beta decay [15]. Therefore, the methods for neutron production are limited, they are based on either spontaneous fission or on a nuclear reaction using incident particles bombarding the nuclei and leading to radioactive decay [15].

2.1.1 Spontaneous Fission

Spontaneous fission refers to the fission that occurs within an atomic nucleus without particle bombardment or any addition of external energy. Spontaneous fission has a higher probability to occur with transuranic heavy nuclides. This process occurs when a heavy nucleus splits into two or more smaller fragments and simultaneously emits neutrons and releases some energy.

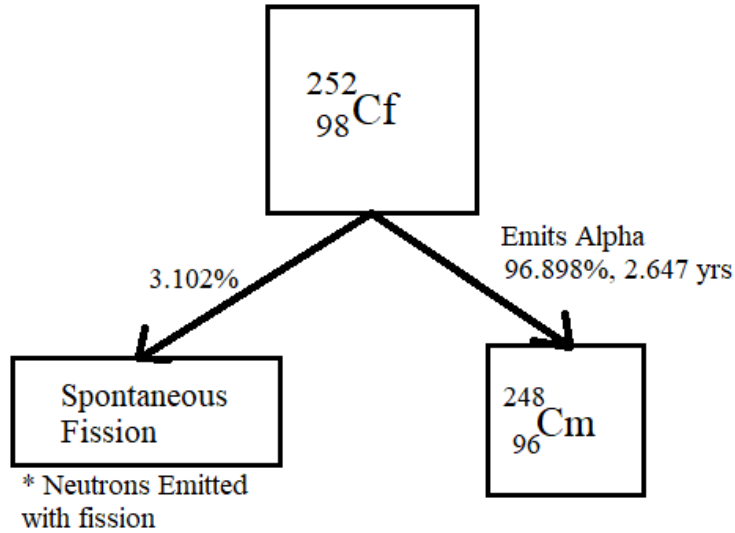
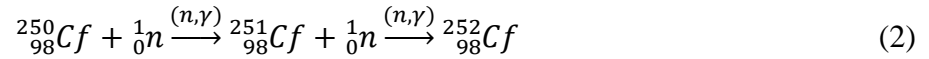
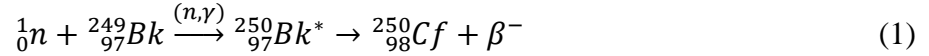


Figure 2.1: ^{252}Cf Decay scheme with probabilities [16].

Californium (^{252}Cf) is the most extensively used spontaneous fission source, which is a 100% artificial element manufactured through nuclear reaction processes. As shown in the ^{252}Cf scheme in Figure 2.1, 96.898 percent of ^{252}Cf decays to ^{248}Cm through alpha decay, but it also has a significant spontaneous fission decay probability of 3.102 percent, which means for every 312 alpha particles emitted from ^{252}Cf , there are roughly 10 fissions that will occur. ^{252}Cf has its neutron yield of around 0.116 neutrons per second per becquerel and specific activity of 2×10^{13} Bq/g, in other words, every microgram of fresh ^{252}Cf can produce 2.30×10^6 neutrons per second with an average energy of 2.1 MeV, which means it can be encapsulated into a very small size container and be used in variety of applications such as reactor start-up rods, material scanners, cancer treatment, and so on [15, 17]. ^{252}Cf is produced using High Flux Isotopes Reactors (HFIR), by bombarding Berkelium-249 with neutrons to form Berkelium-250 [17]. This element has a short half-life ($T_{1/2} = 3.212$ hours) and produces ^{250}Cf through beta negative (β^-) decay. With further

neutron capture, ^{252}Cf is produced inside the reactor. The reaction equations are as illustrated in Equations 1 and 2:



2.1.2 Radioisotope Based Source (α , n) Reactions

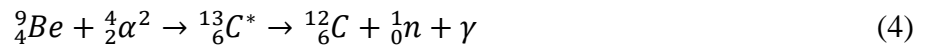
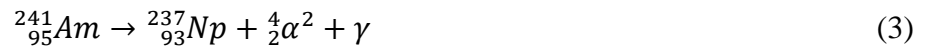
Energetic alpha particles are generated through the decay of heavy radionuclides, which interact with a target nucleus through an (α , n) reaction, which produces the neutron(s) [15]. Due to their high interaction rate, alpha particles can lose their energy prior to reaching any target nuclei. This makes it important to minimize the distance between the emitters and the targets when designing neutron sources. Therefore, the method of designing a radioisotope source is usually to mix alpha particle emitters within the target material; either in the form of an alloy or a ceramic compound [14]. This is then surrounded by a shielded container.

Table 2.1: Characteristics of Be (α , n) neutron sources[15]

Source	Half-Life	E_α (MeV)	Neutron Yield per 10^6 Primary Alpha Particles		Percent Yield with $E_n < 1.5$ MeV	
			Calculated	Experimental	Calculated	Experimental
$^{239}\text{Pu}/\text{Be}$	24000 y	5.14	65	57	11	9-13
$^{210}\text{Po}/\text{Be}$	138 d	5.30	73	69	13	12
$^{238}\text{Pu}/\text{Be}$	87.4 y	5.48	79 ^a	-	-	-
$^{241}\text{Am}/\text{Be}$	433 y	5.48	82	70	14	15-23
$^{244}\text{Cm}/\text{Be}$	18 y	5.79	100 ^b	-	18	29
$^{242}\text{Cm}/\text{Be}$	162 d	6.10	118	106	22	26
$^{226}\text{Ra}/\text{Be}$ + daughters	1602 y	Multiple	502	-	26	33-38
$^{227}\text{Ac}/\text{Be}$	21.6 y	Multiple	702	-	28	38

+ daughters						
-------------	--	--	--	--	--	--

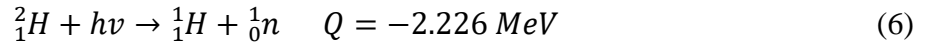
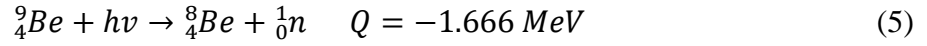
As shown in Table 2.1, the alpha radionuclides used to generate the (α , n) reactions include, Polonium-210, Radium-226, Plutonium-238 (239), Americium-241, and so on. The most commonly used target material is beryllium-9 due to it has a high neutron yield. Compared to the other reactions, $^{226}\text{Ra}/\text{Be}$ and $^{227}\text{Ac}/\text{Be}$ reactions have long chains of daughter products, as well as, the production of a large number of gamma radiation, which results in significant noise. This makes these two sources not suitable for many experiments [15]. The (α , n) reaction neutron sources are usually built in small shielded containers. They can either be designed for long or short term usage depending on the desired application [15]. A common example of an (α , n) reaction neutron source is an AmBe source. There are two nuclear reactions inside an AmBe source. It begins with the spontaneous decay of ^{241}Am , producing alpha particles, which then bombard the ^9Be atoms, resulting in neutrons being emitted [18]. Therefore, the reaction equations defining this neutron source is given in Equations 3 and 4:



2.1.3 Photoneutron Sources (γ , n) Reaction

Neutrons can be produced by (γ , n) reactions through photon interaction with specific light element nuclei if the energy of the photon is greater than the binding energy of the nuclei. Two target nuclei $^2_1\text{H}(\gamma, n)^1_1\text{H}$ and $^9_4\text{Be}(\gamma, n)^8_4\text{Be}$ have the threshold energy of 1.666 MeV and 2.226

MeV respectively. These are the only two target nuclei that are used due to their low threshold energy, all other nuclei have too high of a threshold energy to be practically used. These two reactions are presented in Equations 5 and 6 with their respective reaction quotient value (Q) given beside them:



The energy of the incident photon must be at least equal to or greater than the negative of the Q-value to make the (γ , n) reaction occur. The emitted neutron energy can be calculated using Equation 7 [15]:

$$E_n(\theta) = \frac{M(E_\gamma + Q)}{m + M} + \frac{E_\gamma [(2mM)(m + M)(E_\gamma + Q)]^{\frac{1}{2}}}{(m + M)^2} \cos \theta \quad (\text{For } E_\gamma < 931 \text{ MeV}) \quad (7)$$

In which,

θ is the angle of interaction,

E_γ is the gamma's energy, keV

M is the mass of the recoiled nucleus * c^2 , keV

m is the mass of the neutron * c^2 , keV

Q is the reaction quotient, keV

According to the equation, the second term has little effect on the resulting neutron energy since the angle of θ is changing from 0 to π [15]. As a result, when the initial photons are monoenergetic, the resultant emitted neutrons are nearly monoenergetic. Therefore, the resultant spectrum will display a single clear peak. Few radionuclides are capable of emitting the required

high-energy gamma radiation, and even fewer have an acceptable half-life for neutron sources. The common gamma-ray emitters are Sodium-24, Yttrium-88, Antimony-124, Lanthanum-140, and Radium-226 [15]. Furthermore, for every 10^5 to 10^6 gamma rays emitted, only approximately 1 neutron is produced. Therefore, a significant amount of gamma rays are required to produce a usable amount of neutrons, thus resulting in a high amount of background radiation [15]. Lastly, due to the gamma-ray emitters having short half-lives after irradiation in the reactor, it requires the laboratory facility located close to the reactor [15].

2.1.4 Fusion Sources

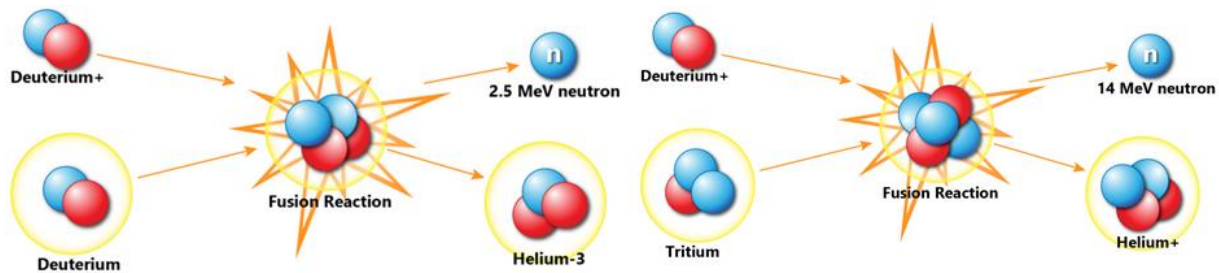
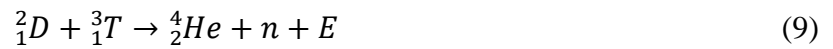


Figure 2.2: D-D and D-T neutron generation [19].

Fusion reactions are composed of two light nuclei, normally hydrogen and its isotopes as shown in Figure 2.2, accelerated to merge and form a heavy nucleus in an excited state. Afterwards, a monoenergetic neutron is emitted along with an atomic nuclei. Deuteron contains one proton and one neutron with an average binding energy of 1.11 MeV and tritium has one more neutron with an average binding energy of 8.48 MeV. The deuteron and tritium have less electric charge, therefore, the coulomb forces between them are smaller compare with other elements. This results in them requiring less energy (about 100~300 keV for deuterium) to overcome the repulsion [15].

Therefore, a charged particle accelerator could provide such energy [20]. The (D, D) and (D, T) reactions occur when either; two deuterium, or one deuterium and one tritium atoms, fuse together and form a helium atom and a fast neutron with an energy of 2.5 or 14 MeV respectively. The two reactions are presented within Equations 8 and 9:



2.2 Neutron Interaction

Since neutrons are chargeless they do not interact with coulomb forces, thus they do not interact with an atom's electric field, and instead can only interact with the nucleus of an atom through nuclear forces. However, since the nucleus makes up approximately 10^{-5} of the volume of the entire atom, they have a relatively low probability of interaction compared to charged particles resulting in them being able to travel multiple centimeters within matter before stopping [21]. Neutron's can have a variety of energy depending on the source, and can be categorized as: Thermal ($0 < E < 0.0025$ eV), Slow ($0.0025 < E < 1000$ eV), Intermediate ($1 < E < 500$ keV), Fast ($0.5 < E < 10$ MeV), and High Energy ($E > 10$ MeV)[2].

Table 2.2: Neutron interaction methods

Neutron Scattering		Neutron Absorption		
Elastic Scattering	Inelastic Scattering	Radiative Capture	Transmutation (n, x) Reaction	Fission Reaction
$A(n, n)A$	$A(n, n)A^*$	$A(n, \gamma)A+1$	$(n, \alpha), (n, p), (n, 2n)$	(n, ffs)

Once the neutron interacts with the nucleus it can either be scattered or absorbed. The different methods of neutron interaction are given in the Table 2.2, more information relating to each method is given below.

2.2.1 Elastic Scattering

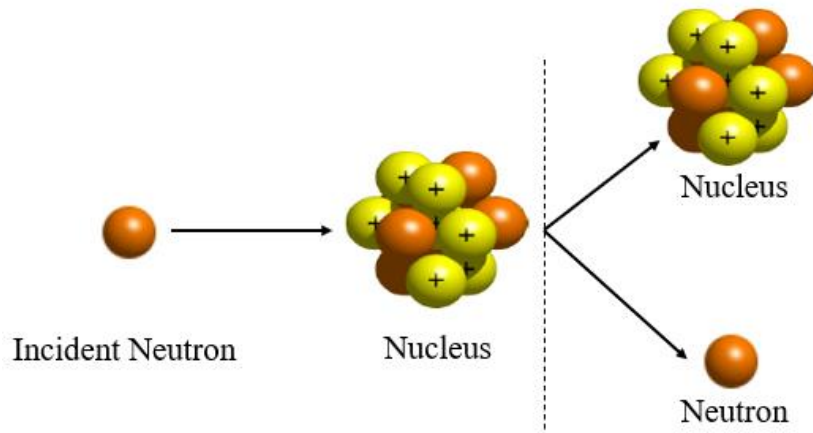
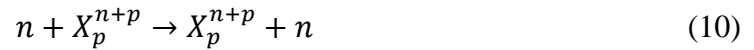


Figure 2.3: Neutron elastic scattering schematic and reaction.



Elastic neutron scattering can occur when a neutron collides with the nucleus of an atom and deflects in a different direction while the total energy of the system that is maintained, as shown in Figure 2.3 and Equation 10. There are two possible elastic neutron scattering modes, potential elastic and resonance elastic. Potential elastic scattering refers to the incident neutron interacting with the nucleus through nuclear forces and is repelled away from the nucleus [22]. Resonance elastic scattering refers to the incident neutron being absorbed by the nucleus, resulting in it transferring its kinetic energy to another neutron inside the nucleus and emitting that one instead [22].

2.2.2 Inelastic Scattering

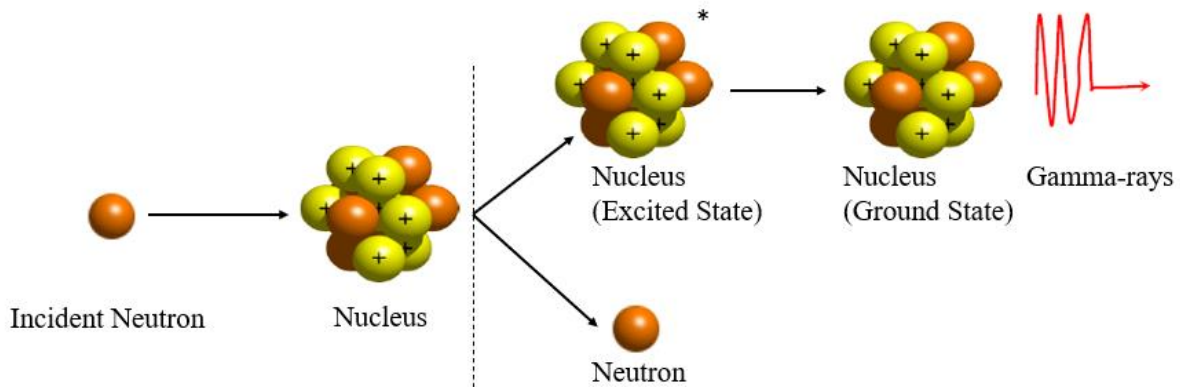
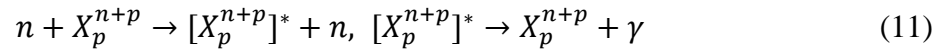


Figure 2.4: Neutron inelastic scattering schematic and reaction.



Inelastic neutron scattering has a similar process as resonance elastic scattering, however, unlike with elastic scattering where the total kinetic energy of the neutron and the nucleus remain constant throughout the interaction, the neutron deposits some of its energy into the nucleus causing the nucleus to enter into an excited state. The neutron then leaves the nucleus with less kinetic energy than before, and a gamma is emitted from the nucleus in order for it to reach ground state as shown in Figure 2.4 and Equation 11 [22].

2.2.3 Radiative Capture

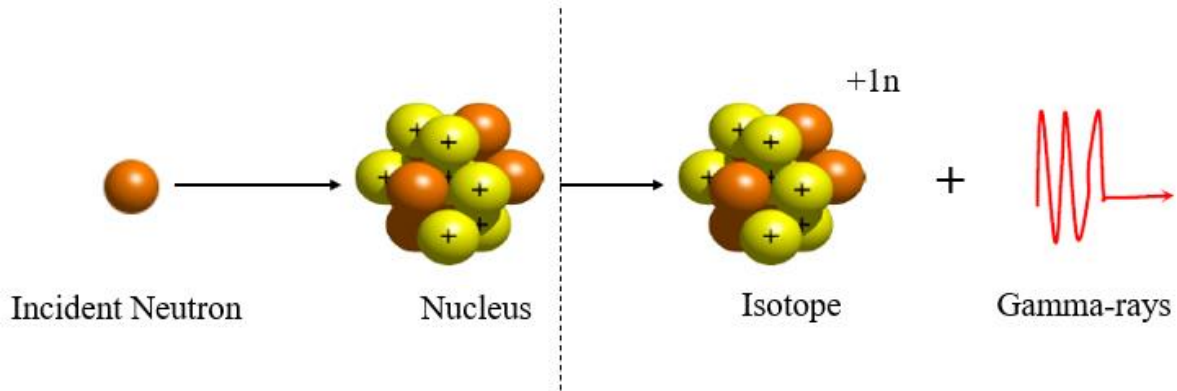


Figure 2.5: Neutron Radiative Capture Schematic and Reaction.

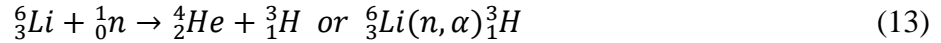


Radiative capture can occur when a neutron collides with a nucleus and is absorbed, causing the nucleus to enter an excited state, which results in gamma decay releasing gamma radiation in order to reach ground state [22]. Radiative capture is a common method for the formation of isotopes which can be seen in Figure 2.6 and Equation 12 [22].

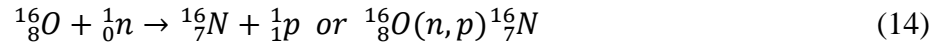
2.2.4 Transmutation (n, x) Reaction

Neutron transmutation is similar to radiative capture in which a neutron collides and is absorbed into the nucleus of an atom, but instead of only releasing gamma radiation it becomes an entirely different element through the release of another type of particle [22]. The x in (n, x) reactions represents all other types of particles that may be emitted from the reaction. Some common reactions are listed in Equations 13 and 14:

Emission of α particles (n, α) Reaction:

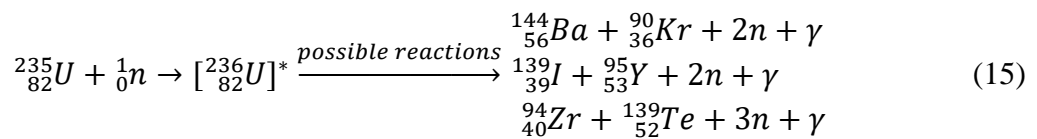


Emission of proton (n, p) reaction:



2.2.5 Fission Reaction

A fission reaction can occur when the incident neutron is absorbed by a heavy element's nucleus. The nucleus initially gets excited then splits into two smaller fragments with the emission of several neutrons and gamma-rays. For example, once an uranium-235 atom absorbs a neutron it becomes an excited uranium-236 atom, which results in it splitting into two fragments with atomic numbers around 95 and 140 [22, 23]. Different fragment pairs have different probabilities of occurring, with some of the more probable ones being, Ba-Kr, I-Y, and Zr-Te [22, 23]. Possible reactions of Uranium-236 are listed in Equation 15:



Fission reactions are the primary type of neutron interaction for current nuclear reactors for the purpose of power generation. Through fission, neutrons are emitted allowing for chain fission reactions to occur if these neutrons cause further fission reactions [22]. This process is controlled within nuclear reactors with the goal to have 1 fission reaction cause 1 new fission reaction. When this occurs a reactor is considered critical.

2.3 Neutron Cross-section

One useful property of a neutron interaction is the microscopic cross-section (σ), which defines the probability of the reaction between a neutron and the effective target area of a single nucleus, and is expressed with the unit of barn ($1 \text{ barn} = 10^{-24} \text{ cm}^2$) [24]. The greater the value of the microscopic cross-section the higher probability that a neutron will interact with the material. The classification of the microscopic cross-section is based on the type of neutron interaction. All cross-sections are energy dependent, as shown below in Figure 2.7, and is the result of the energy corresponding with the neutron velocity [24].

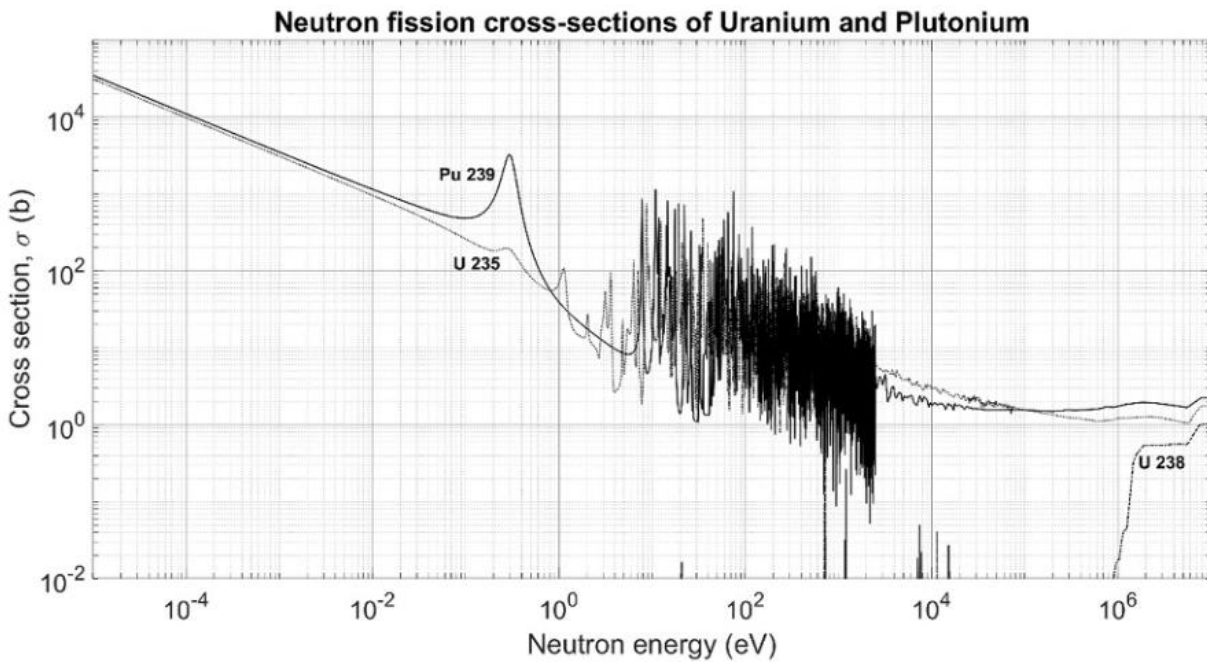


Figure 2.6: Fission cross-section of U-235 and Pu-239 [25].

The sum of the neutron's elastic and inelastic microscopic scattering cross-sections is called the scattering microscopic cross-section, as seen in Equation 16 [24]:

$$\sigma_{scattering} = \sigma_{elastic} + \sigma_{inelastic} \quad (16)$$

Similarly, the sum of the neutron's radiative capture, transmutation, and fission microscopic cross-sections result in the absorption microscopic cross-section, as seen in Equation 17 [24]:

$$\sigma_{absorption} = \sigma_{radiative\ capture} + \sigma_{transmutation} + \sigma_{fission} \quad (17)$$

The sum of the scattering and absorption microscopic cross-sections is called the total neutron microscopic cross-section (σ_{total}) [21]. By multiplying the total neutron microscopic cross-section with the atomic density of the target material, the macroscopic cross-section (Σ) can be calculated, as seen in Equation 18 [25]. The atomic density of a target material can be calculated using the materials density and atomic weight, as seen in Equation 19 [25]. Macroscopic cross-sections are used to present the probability of all neutron interactions that can occur per unit path length within the target material [25].

$$\Sigma = N * \sigma_{total} \quad N = \frac{\rho}{A} * N_A \quad (18) (19)$$

In which,

Σ is the macroscopic cross-section, cm^{-1}

σ is the microscopic cross-section, cm^2

N is the atomic density, cm^{-3}

ρ is the material density, $\text{g}\cdot\text{cm}^{-3}$

A is the atomic weight, $\text{g}\cdot\text{mol}^{-1}$

N_A is Avogadro's number 6.02214×10^{23} , mol^{-1}

If the initial intensity of a neutron beam is known along with the macroscopic cross-section and thickness of the target material, the attenuated intensity of a narrow beam travelling through any material can be calculated using the Beer-Lambert's law, as seen in Equation 20 [24]:

$$I = I_0 e^{-\Sigma d} \quad (20)$$

In which,

I is the attenuated intensity, $\text{neutrons} \cdot \text{s}^{-1}$

I_0 is the initial intensity, $\text{neutrons} \cdot \text{s}^{-1}$

Σ is the macroscopic cross-section, cm^{-1}

d is the thickness, cm

When the thickness and neutron intensity remains constant, the attenuated intensity becomes dependent on the macroscopic cross-section of the material. Therefore, high neutron cross-section material such as baron, cadmium, gadolinium, and hydrogen based materials (like water and paraffin) are preferable to use for neutron shielding. If neutron intensity is known, the neutron flux and reaction rate can be determined using Equations 21 and 22 [25]:

$$\varphi = \frac{I}{A} \quad \text{and} \quad R = N * \sigma * \varphi \quad (21) (22)$$

In which,

φ is the neutron flux, $\text{neutrons} \cdot \text{cm}^{-2} \cdot \text{s}^{-1}$

I is the initial intensity, neutrons*s⁻¹

A is the cross sectional area of interaction between the neutron beam and the material, cm²

σ is the microscopic cross-section, cm²

N is the atomic density, cm⁻³

R is the reaction rate, number of interactions*cm⁻³*s⁻¹

2.4 Neutron Detector Properties

Neutron detectors have a variety of properties that can significantly impact the purpose and procedure of operation. These properties include, mechanisms in which they detect neutrons, operating modes, resolution, efficiency, dead time, etc.

2.4.1 Neutron Detector Mechanisms

The mechanisms in which most neutron detectors measure the number of neutrons are through the secondary radiation that is emitted after interaction with the detectors material. When a neutron interacts with an atom of the detector, the atom becomes excited, and can either emit ionizing radiation or photons [26]. Certain detectors operate by measuring the ionizing radiation, while other detectors measure the photons, and as such, are classified as either proportional or scintillation based detectors respectively. The type of secondary particles that are emitted depend on the type of neutron interaction, either absorption or scattering [26]. As such, detectors will be designed with materials that either promote absorption or scattering depending on their desired type. Scintillation based detectors rely on the production of photons, which then can be detected by a photomultiplier tube (PMT) [27]. PMTs are designed to a photocathode and an anode within a vacuum glass tube with multiple dynode stages. Once the light hits the photocathode, it gets excited and emits photoelectrons into the vacuum. These photoelectrons enter the multiplication system and are amplified by secondary emission through dynodes, and the amplified electrons are then collected as an electronic signal output by the anode [28]. Proportional neutron detectors rely on the production of ionizing radiation within an ion chamber, which collects the electrons and ions at the anode and cathode respectively measuring a pulse or current [27].

2.4.2 Detector Operation Modes

The three general modes for radiation detector operation are, pulse mode, current mode, and Mean Square Voltage (MSV) mode. Pulse mode only detects individual particles and provides better information on the amplitude and a single event timing. The output of the pulse mode normally shows as a series of single peaks, each peak represents an individual interaction within the detector [26]. Current mode measures the average rate of particle interaction within the detector over a period of time and outputs a continuous curve. The average current is measured by current measuring circuits which are installed across the detector [29]. MSV mode can measure different types of radiation simultaneously with the output containing different peaks and is useful when measuring radiation in a mixed radiation environment.

2.4.3 Energy Resolution

Energy resolution refers to the minimum energy interval that the detector can determine between two incident particles with different energies, which can be described as the ability of the detector to distinguish between two peaks [27]. The detector resolution varies between different types of detector and with different absorber materials. The resolution can be calculated by dividing the Full Width at Half Maximum (FWHM) of the peak with the channel or energy at that peak. This relationship can be seen in Equation 23.

$$R = \frac{FWHM}{H_0} \quad (23)$$

Which,

R is the energy resolution of the peak

FWHM is the full width at half maximum channel/energy

H_0 is the peak's channel/energy

Therefore, for the same measurement, a tall and narrow peak has a higher resolution than a short and wide one. There are three main sources of fluctuation in a detector's resolution; the drift during measurement due to the detector's operating characteristics, random noise such as background radiation, and statistical noise [27]. Statistical noise is the dominant source of fluctuations within a detector's resolution, which limits detector performance and cannot be avoided or predicted.

2.4.4 Detection Efficiency

Detection efficiency refers to the ability of a detector to measure the number of recorded particles or photons that have interacted with the detector. There are two types of efficiencies, absolute efficiency and intrinsic efficiency [27]. Absolute efficiency describes the number of pulses that are detected by the detector compared to the number of particles emitted by the sources. It is not influenced by any properties of the detector, instead influenced by the geometry of the sources relative to the detector, primarily the distance between the two unless they are very close together, in which, the shape of the sources and detectors become significant [26]. Since neutrons have generally lower interaction rates compared to other types of radiation, it is necessary to know the absolute efficiency in order to relate the number of counted pulses to the number of incident particles on the detector [27]. Intrinsic efficiency describes the number of pulses recorded by the

detector compare to the radiation quanta incident on the detector. This is heavily impacted by the qualities of the detector. Their equations are given in Equations 24 and 25 respectively [27].

$$\varepsilon_{abs} = \frac{\text{Number of Pulses Recorded}}{\text{Number of Radiation Quanta Emitted by Source}} \quad (24)$$

$$\varepsilon_{int} = \frac{\text{Number of Pulses Recorded}}{\text{Number of Radiation Quanta Incident on Detector}} \quad (25)$$

For isotropic sources, these two efficiencies are related using Equation 26[27].

$$\varepsilon_{int} = \varepsilon_{abs} \left(\frac{4\pi}{\Omega} \right) , \quad \Omega = \int_A \frac{\cos \alpha}{r^2} dA \quad (26)$$

In which,

Ω is the solid angle of the detector from the source position

r is the distance between source and detector surface

α is the angle between the normal of the detector surface and the source's direction

dA is the detector surface element

Since not all interactions within the detector deposit all of their energy, peak efficiency can be useful to describe the number of pulses that fully deposit all of their energy into the detector versus the number of particles incident on the detector, as seen in Equation 27 [27].

$$\varepsilon_{ip} = \frac{\text{Number of Pulses Recorded under a Peak}}{\text{Number of Particles Incident on Detector}} \quad (27)$$

2.4.5 Dead Time

Dead time is the result of a physical process occurring within the detector and is an intrinsic feature of the detector. It describes the minimum amount of time that a detector requires to separate between successive events in order to be detected as two separate pulses [26]. It is a result of the time required for the detector to process the incident neutron interaction into a measured pulse, and is described using τ . Any pulses incident on the detector during the dead time resulting from another particle cannot be recorded. This is a common occurrence due to the random nature of radioactive decay, and can significantly impact the overall output of a detector depending on the sources activity [27]. With higher source activity, dead time becomes more important to calculate as there will be an increase in error of the results. The length of the dead time can either be set to a specific value, or set to the minimum dead time of the detector based on its intrinsic features [26]. In certain cases, higher dead time can help further discriminate between different activity sources in multi-radiation environments.

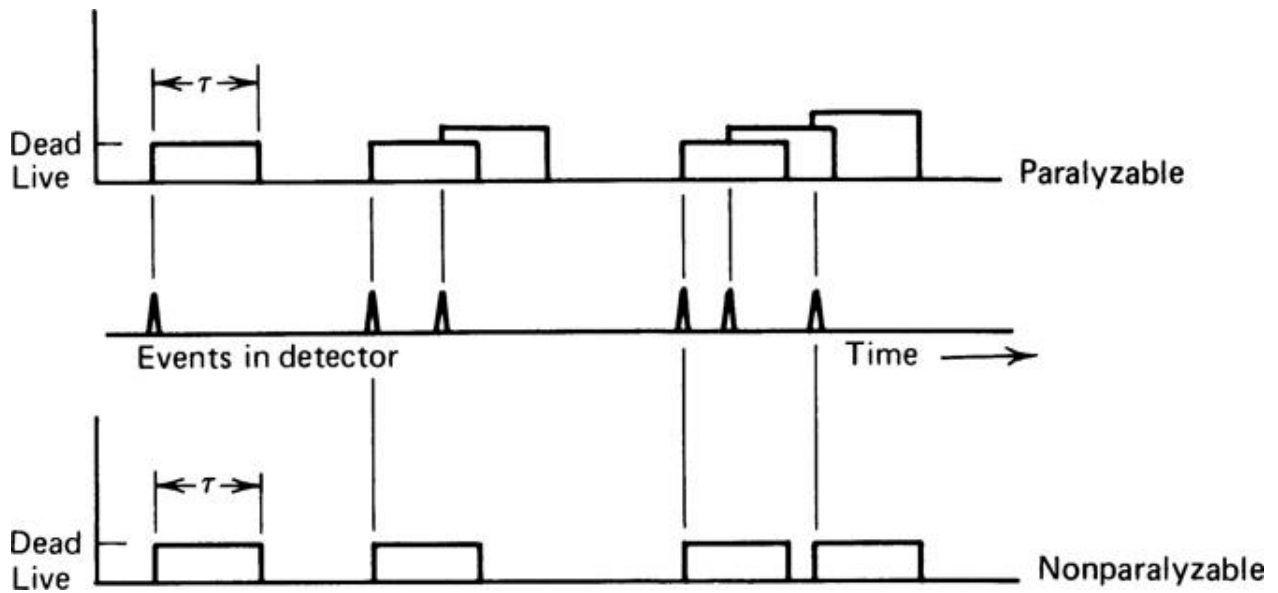


Figure 2.7: Two dead time models[26].

There are two dead time response models commonly used for counting systems, paralyzable and nonparalyzable [26]. For the paralyzable model, when a particle interacts with the detector during another particles dead time, additional time is added without recording the pulse [26]. Conversely, for the nonparalyzable model, instead of extending the duration of dead time, the second particle is completely ignored [26]. At low source activity both models are behave similarly, but at higher source activities the paralyzable model can result in extended periods of dead time, where it is not recording a significant number of counts [26]. Both models are illustrated in Figure 2.8 and display the difference in the number of counts that are recorded. For the paralyzable model only 3 of the 6 counts were recorded, while, the unparalyzable model was able to record 4 counts. Generally, real-life counting systems have their behavior as an intermediate between these two models [26].

Since dead time cannot be avoided, a method to correct the measured data is necessary. If the activity of the source of radiation is steady, and the counting time is long enough, Equations 28 and 29 can be used for calculating the dead time for paralyzable and nonparalyzable models respectively [27]:

$$m = ne^{-n\tau} \quad , \quad n - m = nm\tau \quad (28) \quad (29)$$

In which,

n is the true interaction rate

m is the recorded count rate

τ is the system's dead time, s

For the paralyzable model the true interaction rate cannot be calculated due to the fact that it cannot be isolated in the equation [27]. This equation can be only used when the n value is given.

2.5 Common Neutron Detectors

There are four types of neutron detectors: gas proportional, scintillation, semiconductor, and activation, which are categorized by their neutron interactions. Among these detectors, gas proportional and scintillation neutron detectors are the two most common detectors that used for neutron detection. Semiconductor neutron detectors are a recent technology, and as such, are not widely used within the industry yet. Neutron activation detectors uses the Neutron Activation Analysis (NAA) method which requires a high output of neutrons. Most neutron detectors are designed for the detection of slow neutrons using materials with a high cross section at low neutron energies. Since materials that have a high cross section at low energies usually have a low cross section at high energies, most detectors used for slow neutrons are not suitable for fast neutron detection.

2.5.1 Slow Neutron Detection

There are three main factors to consider when designing a slow neutron detector. Firstly, the neutron interaction cross-section should be as high as possible to increase the detector efficiency, conversely minimizing the detector dimensions [28]. Secondly, the Q-value of the neutron interaction should be high enough to discriminate between the neutron and secondarily generated gamma radiation which can also ionize the detectors gas [28]. Lastly, the ability of the detector to transfer kinetic energy of the secondary charge particles to the material within the detector in order to deposit all of the particles energy [28]. Depending on the material the range of the charged particles can be significant in the design of the detector [28].

For current slow neutron detection gas proportional detectors are primarily used, which rely on the generation of heavy charged particles (recoil nucleus, proton, alpha particle, and fission fragments) produced by neutron absorption [28]. The three most popular reactions used for slow neutron detection are $^{10}\text{B}(n, \alpha)$ reaction, $^6\text{Li}(n, \alpha)$ reaction, and $^3\text{He}(n, p)$ reaction.

Table 2.3: Properties of $^{10}\text{B}(n, \alpha)$, $^6\text{Li}(n, \alpha)$, and $^3\text{He}(n, p)$ reactions. (Data from [28])

	$^{10}\text{B}(n, \alpha)$		$^6\text{Li}(n, \alpha)$	$^3\text{He}(n, p)$
Abundance	19.9%		7.6%	0.0014%
Thermal Neutron Cross-section	3837 barns		937 barns	5330 barns
Reaction	$^{10}_5\text{B} + {}^1_0\text{n} \rightarrow$	${}^7_3\text{Li} + {}^4_2\alpha$ (6%)	${}^6_3\text{Li} + {}^1_0\text{n} \rightarrow {}^3_1\text{H} + {}^4_2\alpha$	${}^3_2\text{He} + {}^1_0\text{n} \rightarrow {}^3_1\text{H} + {}^1_1\text{p}$
		$[{}^7_3\text{Li}]^* + {}^4_2\alpha$ (94%)		
Q-value	2.79 MeV, 2.31 MeV		4.78 MeV	0.76 MeV
Kinetic Energy (E)	$\alpha = 1.47$ MeV		$\alpha = 2.05$ MeV	$\text{p} = 0.57$ MeV
	${}^7\text{Li} = 0.84$ MeV		${}^3\text{H} = 2.73$ MeV	${}^3\text{H} = 0.19$ MeV

Table 2.3 displays the main parameters of the three common reactions for slow neutron detection. All three reactions show a substantial thermal neutron cross-section for neutron interaction. $^3\text{He}(n, p)$ reaction has a much higher thermal cross-section compared to the other two reactions, however, due to global shortage and high cost of the production, ^3He is not commercially friendly for some applications. $^6\text{Li}(n, \alpha)$ reaction has a significantly lower thermal neutron cross-section than the other two reactions, but has a significantly higher Q-value of the reaction. $^{10}\text{B}(n, \alpha)$ is the most popular nuclear reaction for slow neutron detection due to it having a relatively high thermal neutron cross-section and Q-value, a typical BF_3 gas filled proportional counter is widely used as a slow neutron detector.

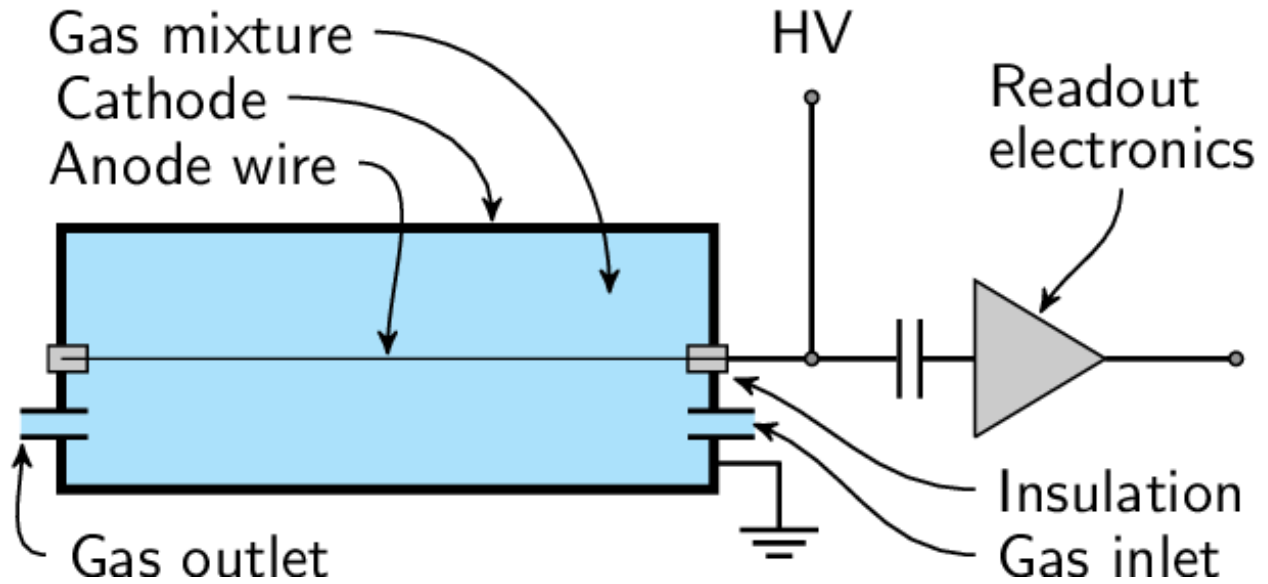


Figure 2.8: Gas filled proportional counter schematic [30].

As shown in Figure 2.9, the structure of the BF_3 gas filled proportional counter consists of a metal cylindrical container with an anode wire placed along the center and the shell acting as the cathode. The working material is a high enriched BF_3 gas that acts as a target nucleus for slow neutron interaction to produce secondary charged particles, as well as, the gas that ionizes due to the generated charged particles. BF_3 contains a high concentration of boron, with an absolute pressure within the detector of approximately 0.5 to 1.0 atmosphere as it is not efficient at a higher pressures [28]. The incident neutron interacts with a ^{10}B nucleus, producing an alpha particle and a ^7Li recoiled nucleus (94% excited state and 6% ground state). These two products proceed to collide with BF_3 gas atoms and deposit their energy ionizing the atom producing electrons and positive ions [28]. Under the electric field, the electrons move toward the central anode wire and the positive ions drift toward the cathode shell with a much slower rate. The electric field surrounding the anode is greater than the electric field around the cathode, resulting in the electrons near the anode wire being accelerated and further ionizing additional BF_3 gas atoms. Once all

positive ions are collected by the cathode, the pulse reaches its full amplitude, resulting in the output pulse from the anode wire being proportional to the initial ionization. Since this detector is used for slow neutrons with low kinetic energy the initial reaction causes the two products to move in the opposite directions from each other, which usually results in one of the products reaching the wall of the detector [28]. As a result, most of the time one particle will leave the detector and only one will be counted on the final spectrum. An example spectrum of a BF_3 gas filled proportional detector is displayed below in Figure 2.10.

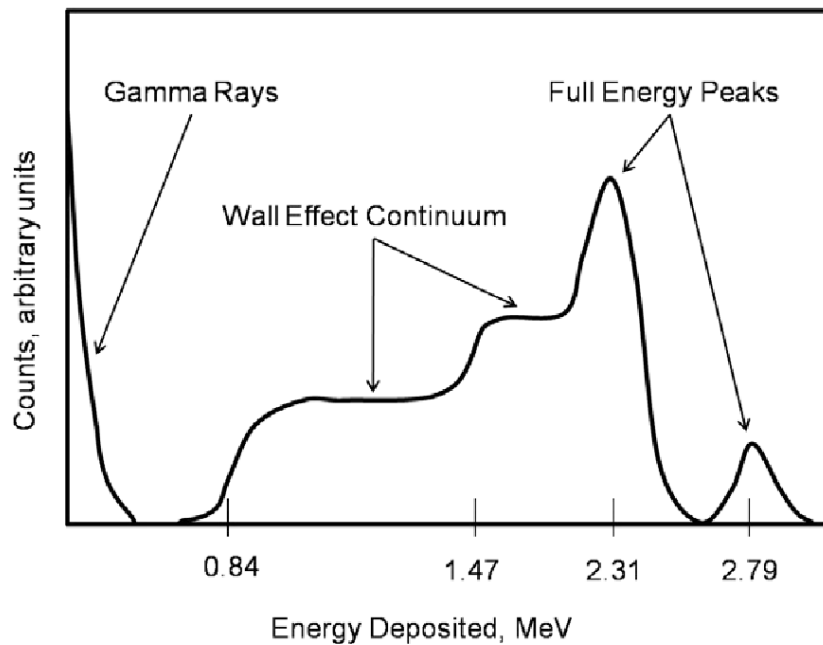


Figure 2.9: BF_3 gas filled proportional counter spectrum[31].

BF_3 gas filled proportional detectors can theoretically be used for fast neutrons, however, ^{10}B has a poor neutron cross-section at high neutron energy, which results in a low efficiency at these energy levels.

2.5.2 Fast Neutron Detection

Fast neutrons are generally produced by reactors through fission chain reactions or accelerators by (D, D) or (D, T) reactions with a range of neutron energy from 0.5 MeV up to tens of MeV and a significantly higher velocity compared to slow neutrons. As a result, the initial neutron kinetic energy is not negligible for fast neutrons compared with the nuclear reaction Q-value [32]. Unlike slow neutron which usually interacts through elastic scattering or neutron capture, fast neutrons typically only interact through elastic scattering with a significantly lower probability for neutron capture. Furthermore, since fast neutrons primarily interact through elastic scattering with a Q-value of zero, this allows for the neutron to transfer more of its energy to the target, especially if the target is a light element such as hydrogen or helium. As a result, multiple types of fast neutron detectors have been designed using different mechanisms to detect neutrons, such as, neutron moderation type, neutron scattering, and neutron reaction.

2.5.2 (a) Neutron Moderation Type Detector

This type of detector works similarly to slow neutron detectors, but an extra step is needed to moderate the neutron before interacting with the detector's material in order to reduce its energy as the materials used for slow neutrons have poor neutron cross sections at high energies [32]. As a result, materials composed mostly of hydrogen atoms, which have a high neutron cross-section, are used as moderators [32]. Polyethylene and paraffin wax are commonly used as a moderator, which increase the detector's overall efficiency. A downside to this type of detector is the fact that it loses information on the initial neutron's energy, and as a result, the source of the neutron.

The most important parameter for this type of detector is the thickness of the moderator used. This thickness needs to be customized to detect a specific neutron energy range. If the thickness is too much, the neutrons will be attenuated too much, with some not being able to reach the detector at all [32]. If the thickness is too little, the inverse occurs, where the neutrons are not attenuated enough resulting in neutrons with too high of energy to be efficiently detected by the detector [32]. Therefore, this type of detector has a maximum efficiency which is balanced according the neutrons energy. An example of a typical spherical detector schematic is shown below in Figure 2.11.

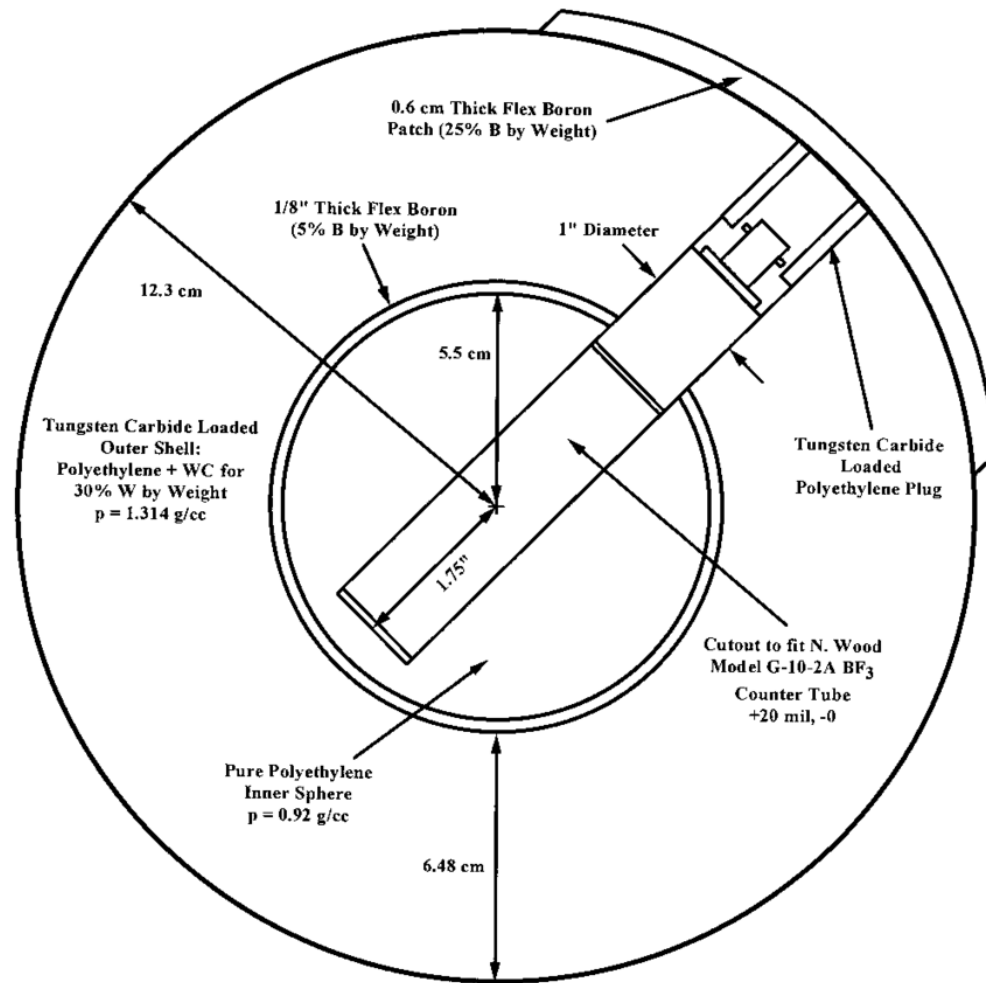


Figure 2.10: Spherical detector schematic[33].

2.5.2 (b) Neutron Scattering Detectors

Unlike the previous detector, this type of detector does not require moderation as it operates by utilizing the high elastic collision probability of fast neutrons along with light elements such as hydrogen, deuterium, and helium to transfer the neutrons energy to the detectors material directly [27]. Once these elements get energized due to the neutron transferring some of its kinetic energy, they begin to ionize or excite the surrounding atoms [32]. The main method of detecting these interactions is through the use of PMTs, but ion chambers can also be used. The equation used to calculate the recoil nucleus kinetic energy is shown in Equation 30 [32]:

$$E_R = \frac{4A}{(1+A)^2} (\cos^2 \theta) E_n \quad (30)$$

In which,

A is the mass of target nucleus divided by the mass of the neutron, amu

E_n is the kinetic energy of incident fast neutron ($E_n < 939 \text{ MeV}$)

E_R is the kinetic energy of the recoil nucleus

θ is the scattering angle of the recoil nucleus, °

According to Equation 30, the maximum kinetic energy transfers at an scattering angle of zero degrees, with the minimum kinetic energy transferring at an scattering angle of ninety degrees. Therefore, the minimum energy transfer approaches 0, while the maximum is dependent on the type of recoil nucleus [32]. As a result, this type of detector is useful when the neutron's energy is significantly high as it can better distinguish between the secondary radiation generated and the background radiation of it environment [32].

2.5.2 (c) Fast Neutron Reaction Based Proportional Detectors

Similar to the proportional detectors used for slow neutrons, fast neutron reaction based proportional detectors rely on the reaction between a fast neutron and a target material with a suitable fast neutron cross-section [32]. ^3He is frequently used as it has a suitable fast neutron cross-section of 1 barn at 0.5 MeV to approximately 0.1 barn at 15 MeV, which is considered good for detectors operating in this energy range [32]. A fast neutron cross section graph for the $^3\text{He}(n, p)$ reaction is shown in Figure 2.12.

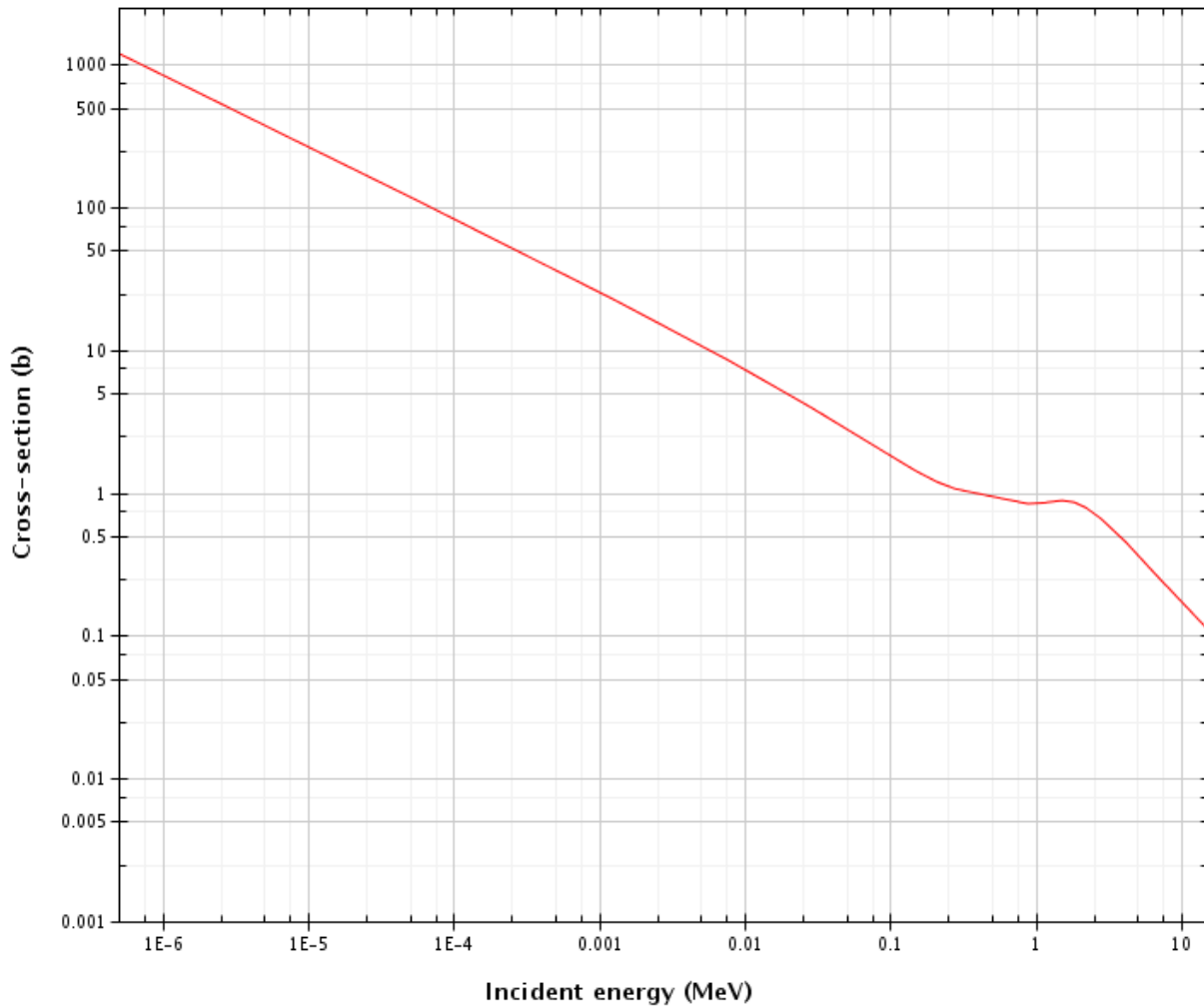


Figure 2.11: Fast neutron cross-section of the $^3\text{He}(n, p)$ reaction [34].

Fast neutron's scattering cross-section is always higher than the cross section of (n, p) reactions, therefore, it is expected to see three distinct features on the pulse spectrum a ^3He detector, a full energy peak where the full energy of the neutron is measured, a recoiled distribution curve resulting from neutron elastic collisions at various angles similar to photon's Compton scattering, and a thermal neutron peak resulting from neutron moderation before detection [32]. One of the common reactions use for fast neutron reaction detector is $^3\text{He}(n, p)$ reaction. This type of detector can be expensive because of the shortage previously explained.

2.6 References

2. Machrafi, R., *Neutron Interaction with Matter*. 2018, Ontario Tech University: Oshawa.
15. Knoll, G.F., *Neutron Sources*, in *Radiation Detection and Measurement, 2nd ed.* 1989, John Wiley and Sons Inc.: United States. p. 20-28.
16. Section, I.N.D., *Parent Daughter Chain*. 2021, IAEA.
17. Corporation, F.T., *Californium-252 (Cf-252) Production*. Frontier Technology Corporation.
18. Machrafi, R., *RADI4430U-Industrial Application of Radiation Techniques Lab Manual*. 2019, Ontario Tech University: Oshawa.
19. Phoenix, *D-D neutron Generator (Deuterium-Deuterium)*. 2021, Phoenix.
20. Ahmed, S.N., *General Properties and Sources of Particles and Waves*, in *Physics and Engineering of Radiation Detection*. 2015, ELSEVIER: AMSTERDAM, BOSTON, HEIDELBERG, LONDON, NEW YORK, OXFORD, PARIS, SAN DIEGO, SAN FRANCISCO, SINGAPORE, SYDNEY, TOKYO. p. 51.
21. Knoll, G.F., *Interaction of Neutrons*, in *Radiation Detection and Measurement, 2nd.* 1989, John Wiley and Sons Inc.: United States. p. 57-59.
22. Ahmed, S.N., *2.6 Interaction of Neutral Particles with Matter*, in *Physics and Engineering of Radiation Detection*. 1989, John Wiley and Sons Inc.: AMSTERDAM, BOSTON, HEIDELBERG, LONDON, NEW YORK, OXFORD, PARIS, SAN DIEGO, SAN FRANCISCO, SINGAPORE, SYDNEY, TOKYO. p. 137-140.
23. Marks, A., et al., *Physics of Uranium and Nuclear Energy*. 2020, World Nuclear Association.

24. Malkapur, S.M. and M.C. Narasimhan, *Virgin and waste polymer incorporated concrete mixes for enhanced neutron radiation shielding characteristics*, in *Use of Recycled Plastics in Eco-efficient Concrete*. 2019, Woodhead Publishing. p. 215-247.
25. Kerlin, T.W. and B.R. Upadhyaya, *7.3 Moderator temperature feedback in thermal reactors*, in *Dynamic and Control of Nuclear Reactor*. 2019, Elsevier Science & Technology: Londo, San Diego, Cambridge, Oxford. p. 76.
26. Knoll, G.F., *General Properties of Radiation Detectors*, in *Radiation Detector and Measurement, 2nd ed.* 1989, John Wiley and Sons Inc.: United States. p. 103-128.
27. Machrafi, R., *Fundamentals of Radiation Detectors*. 2019, Ontario Tech University: Oshawa.
28. Knoll, G.F., *Chapter 14 Slow Neutron Detection Methods*, in *Radiation Detection and Measurement, 2nd ed.* 1989, John Wiely and Sons Inc.: United States. p. 481-493.
29. IAEA, *Reactor Protection System*. 2021, IAWA.
30. Hilden, T., *A gaseous proportional counter built from a conventional aluminum beverage can*. American Journal of Physics, 2013. **83**(8): p. 2.
31. Boyce, N.O., *Thermal Neutron Point Source Imaging using a Rotating Modulation Collimator (RMC)*. 2010, SEMANTIC SCHOLAR.
32. Knoll, G.F., *Chapter 15 Fast Neutron Detection and Spectroscopy*, in *Radiation Detection and measurement, 2nd.* 1989, John Wiley and Sons Inc.: United States. p. 514-549.
33. Olsher, R.H., et al., *WENDI AN IMPROVED NEUTRON REM METER*. Health Physics, 2000. **79**(2): p. 170-181.
34. Web, J., *Incident neutron data / ENDF / B-VII.1 / He3 / MT = 103 : (z,p) / Cross Section*. 2022, JANIS Web.

CHAPTER 3: METHODOLOGY DESCRIPTION

3.1 ^{35}Cl Nuclear Reactions

The detector that is being investigated within this report utilizes ^{35}Cl 's neutron absorption reactions, which have a similar behaviour as ^3He for fast neutrons. When ^{35}Cl interacts with a neutron it has a chance to absorb the neutron undergoing transmutation into ^{36}Cl , which can decay through either of these reactions, $^{36}\text{Cl}(n, p)^{35}\text{S}$ or $^{36}\text{Cl}(n, \alpha)^{32}\text{P}$. The nuclear reaction energy levels of ^{36}Cl , ^{35}S , and ^{32}P are presented in Figure 3.1.

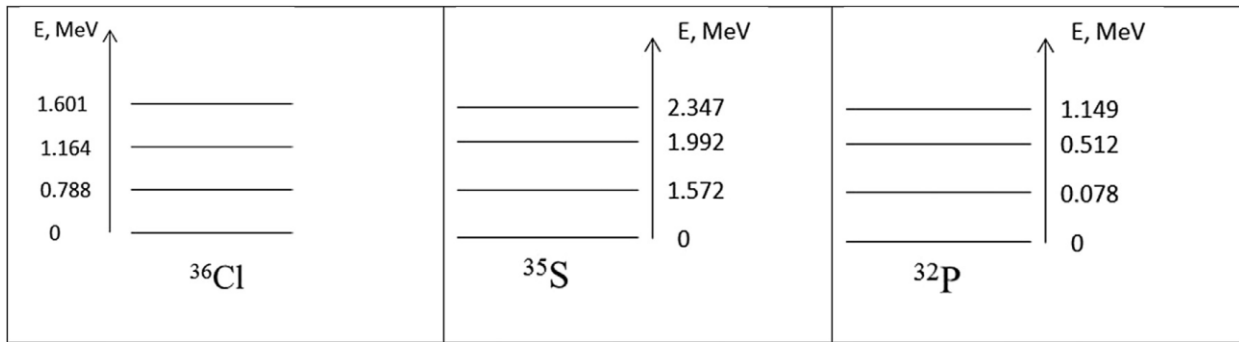


Figure 3.1: Nuclear reaction energy of ^{36}Cl , ^{35}S , and ^{32}P [35].

3.1.1 $^{35}\text{Cl}(n, p)^{35}\text{S}$ Reaction

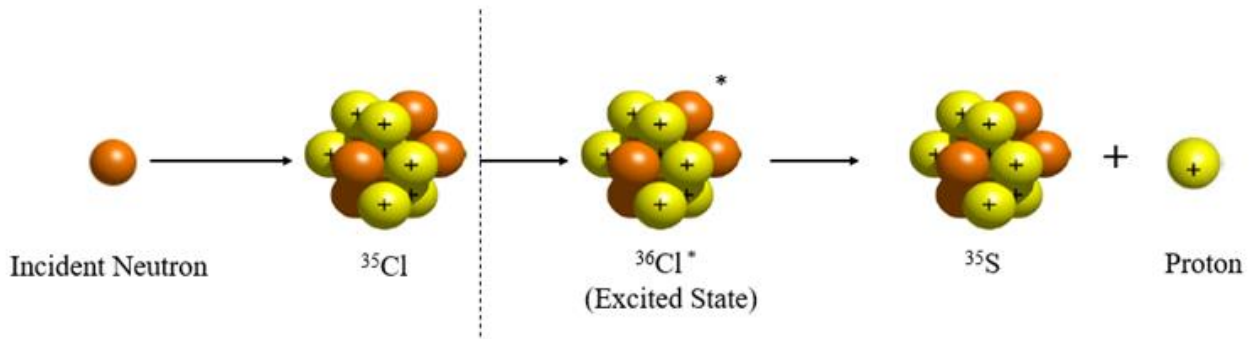


Figure 3.2: Illustration of a $^{35}\text{Cl}(n, p)^{35}\text{S}$ reaction.



As shown in Figure 3.2 and Equation 31, ^{35}Cl absorbs the incident neutron becoming excited to $^{36}\text{Cl}^*$, the excited $^{36}\text{Cl}^*$ then decays to ^{35}S with the emission of a proton. The Q-value of this reaction is approximately 615.22 keV, therefore the energy of the peak can be determined using Equation 32, though this is not always the case due to quenching which will be discussed in section 4.5.

$$E_{\text{Peak}} = Q + E_n \quad (32)$$

In which,

E_{Peak} is the energy of the peak, MeV

Q is the reaction energy, MeV

E_n is the incident neutron energy, MeV

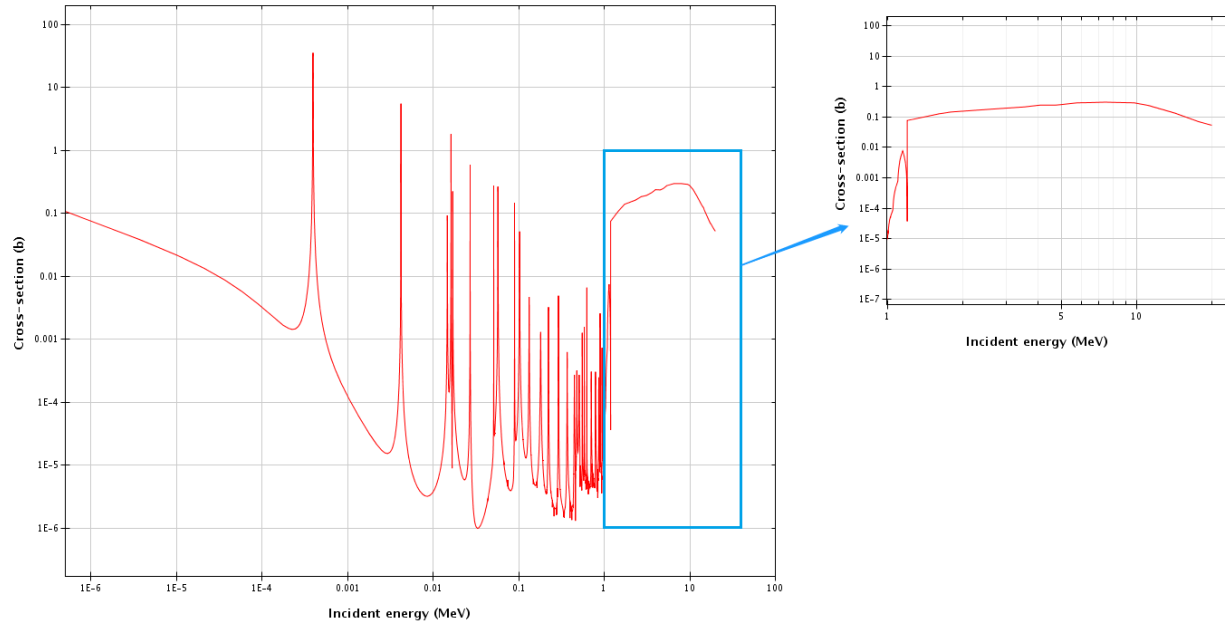


Figure 3.3: $^{35}\text{Cl}(n, p)^{35}\text{S}$ reaction cross-section [36].

The neutron cross-section of a $^{35}\text{Cl}(n, p)$ reaction increases linearly with neutron energy between 1 to 10 MeV as seen in Figure 3.3, which is beneficial for fast neutron spectrometry between this energy range [13].

3.1.2 $^{35}\text{Cl}(n, \alpha)^{32}\text{P}$ Reaction

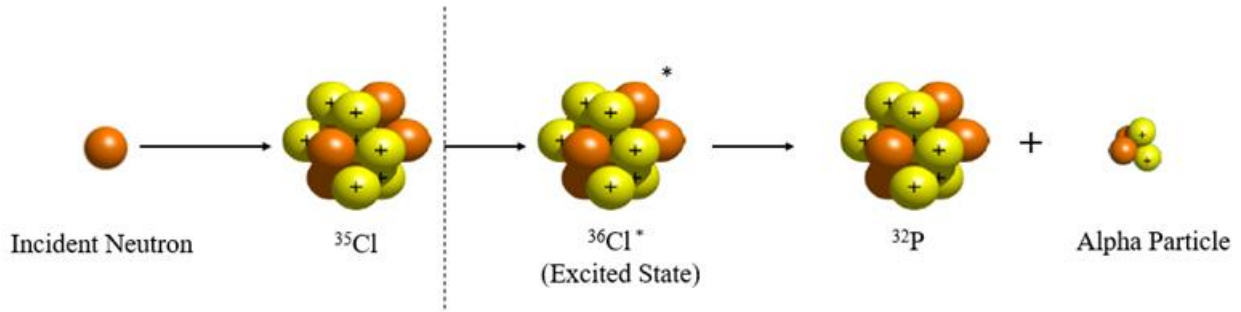
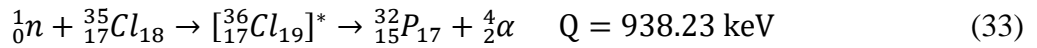


Figure 3.4: Illustration of a $^{35}\text{Cl}(n, \alpha)^{32}\text{P}$ reaction.



As shown in Figure 3.4 and Equation 33, ^{35}Cl absorbs the incident neutron becoming excited to $^{36}\text{Cl}^*$, the excited $^{36}\text{Cl}^*$ then decays to ^{32}P with the emission of an alpha particle. The Q-value of this reaction is approximately 938.23 keV, therefore the energy of the peak can be determined using Equation 32. This reaction will experience more quenching than the previous reaction due to alpha's experiencing more quenching than protons, and will most likely result in both peaks somewhat coinciding with each other [35].

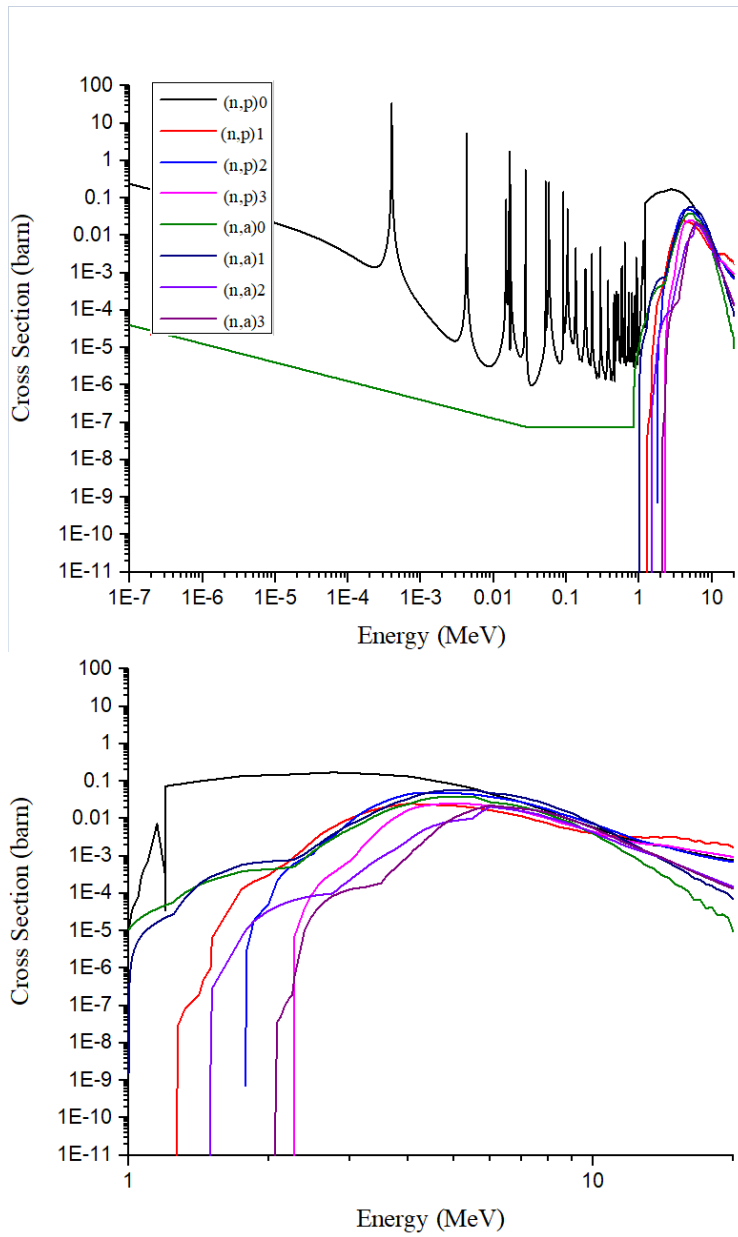


Figure 3.5: Cross-section of $^{35}\text{Cl}(n, p)^{35}\text{S}$ reaction and $^{35}\text{Cl}(n, \alpha)^{32}\text{P}$ reaction [36].

Figure 3.5 presents the cross-sections of $^{35}\text{Cl}(n, p)$ and $^{35}\text{Cl}(n, \alpha)$ reactions at various energy levels. Both reactions have a similar trends of their cross-sections between 1 to 10 MeV, these cross-sections should be significant enough to appear in pulse height spectra. Within Figure 3.5,

the line with the highest cross-section is in black, representing the cross-sections of $^{35}\text{Cl}(n, p_0)$ reactions, therefore, this is the most likely reaction to appear as the prominent peak on a spectrum.

3.2 Monte Carlo Simulation

MCNP is a general-purpose Monte Carlo N-Particle code developed by Los Alamos National Laboratory which can be used to model neutron, photon, electron, and coupled transport radiation calculations [37]. It has a wide range of applications in the fields of radiation protection, shielding design, detector design, and reactor core design [37]. In this thesis, the MCNP/X code was used to model a LaCl_3 scintillating detector to obtain its response functions for gamma and fast neutron interactions within a simulated neutron facility in Ontario Tech University.

3.2.1 MCNP Model

To model an experiment with MCNP, it requires the user to specify the parameters in an input file. There were individual input files for ^{22}Na and the neutron source. Furthermore, the neutron source had multiple input files for each combination of particle. These input files included parameters for geometry specification, materials contained in the model including which cross-section library, source definitions, and type of tallies used to determine the output. Examples of the input code are presented in Appendices B-E.

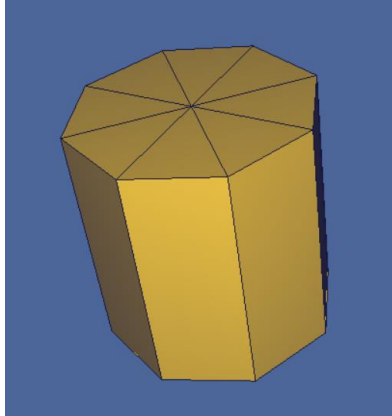


Figure 3.6: MCNP model of the LaCl_3 detector.

A cylindrical 1.5x1.5 inch (1 inch = 2.54 cm) LaCl_3 detector had been simulated using MCNPX as shown in Figure 3.6. This detector had been placed in the center of a neutron facility which was a simulated rectangular room made of one meter thick heavy concrete. The space inside the room was set to be composed of air and the space outside the room to be void. The specific input materials used in the simulations are listed in the Appendices A Table A1-A3. For gamma detection, the gamma source was simulated as a point source and placed at the center of the circular face of the detector. For fast neutron detection, the neutron source was also simulated as a point source but placed 14 cm from the center of the circular surface of the detector. All of the simulations used a F8 tally to simulate the detector to generate the pulse height spectra.

One of the issues with MCNP that appeared was that it does not consider the physical effect of energy broadening, instead, a specific command within the tallies called Gaussian Energy Broadening (GEB) was used to manually adjust the detector resolution in the simulation using experimental data. For example, the detector was adjusted to have a resolution of 5% for ^{22}Na at 511 keV as this was the resolution determined through gamma source experiments.

3.3 Experimental Apparatus

3.3.1 LaCl₃ Scintillator Description

LaCl₃ is an insulator material as it has a conduction and valence electron band with a gap separating the two. When gamma rays with energy greater than the gap traverse LaCl₃ molecules they can undergo core valence luminescence (CVL). This occurs when the gamma ray excites an electron from the valence band into the conduction band, in which the electron will proceed until their energy falls below the conduction band. Within this gap there are luminescence centers, which are energy levels with an energy difference that fall within the visible light electromagnetic spectrum. If the electron jumps to an energy level below the conduction band that is the energy level of a luminescence center, they can jump further to a lower luminescence center, which can either produce a photon, or disperse the energy non-radiatively. This is why it can be used as a scintillating material for gamma radiation. Ce³⁺ can be used as a dopant within scintillating crystals to produce more photons as a result of more luminescence centers. If the crystal is large enough and doped with Ce³⁺ ions, Ce³⁺ prompt can occur, which is when the photons that is emitted from CVL is absorbed by the ions, and re-emitted at a lower wavelength. The recoiled protons that are produced from neutron induced reactions ionize the crystal do not excite the CVL or induce prompt Ce³⁺ emissions, but still produce photons at a later time. This is also used to discriminate between neutron and gamma rays within a mixed field.



Figure 3.7: $\text{LaCl}_3:\text{Ce}$ scintillator crystal[38].

The detector material used in these experiments was a cylindrical 1.5x1.5 inch (1 inch = 2.54 cm) $\text{LaCl}_3:\text{Ce}$ crystal with the model number, 38 S 38/2, from Saint-Gobain Crystals, presented in Figure 3.7. The $\text{LaCl}_3:\text{Ce}$ scintillation crystal has the density of 3.85 g/cm^3 with a light yield of 40,000 photons per MeV of the particle. It has a decay time of less than 28 nanoseconds and a maximum emission wavelength of 350 nanometers [38].

3.3.2 Electronic and Software

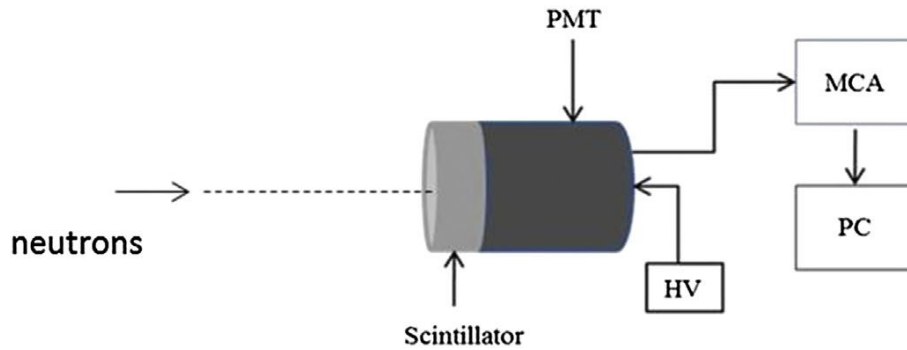


Figure 3.8: Detector schematic.

As presented in Figure 3.8, the detector was composed of a $\text{LaCl}_3:\text{Ce}$ scintillation crystal attached to a 2 inch Hamamatsu R6231 PMT to convert the light into an electrical signal, with the entire assembly encased in a standard aluminum housing [8]. The mechanisms of the PMT is based on the photoelectric effect and production of secondary emissions. PMTs consist of a photocathode, multiple dynodes, and an anode. Once the photons produced by the scintillator interact with the photocathode, the electrons are emitted through the photoelectric effect. The resulting electrons are then accelerated and interact with the first dynode which produce more electrons. This interaction continues through a series of dynodes with increasing voltage until the electrons reach anode where they are then collected. The number of electrons can be correlated to the number of dynodes and the voltage.

A sensor and the PMT were attached to an Osprey universal digital multichannel analyzer (MCA) manufactured by Canberra. This MCA is built as an all-in-one device with a high-voltage power supply, preamplifier, and a full-featured digital pulse processor and MCA [9].

The MCA was connected to a computer with an USB wire to transfer the data for further analyzing. The software used to analyze the output data is Gamma Acquisition & Analysis, this software records the data and plots it into histograms as count(s) vs. channel. In this thesis, the measured data files were saved from Gamma Acquisition & Analysis and exported to OriginPlot for data analysis and graphing, as can be seen in Figure 3.9.

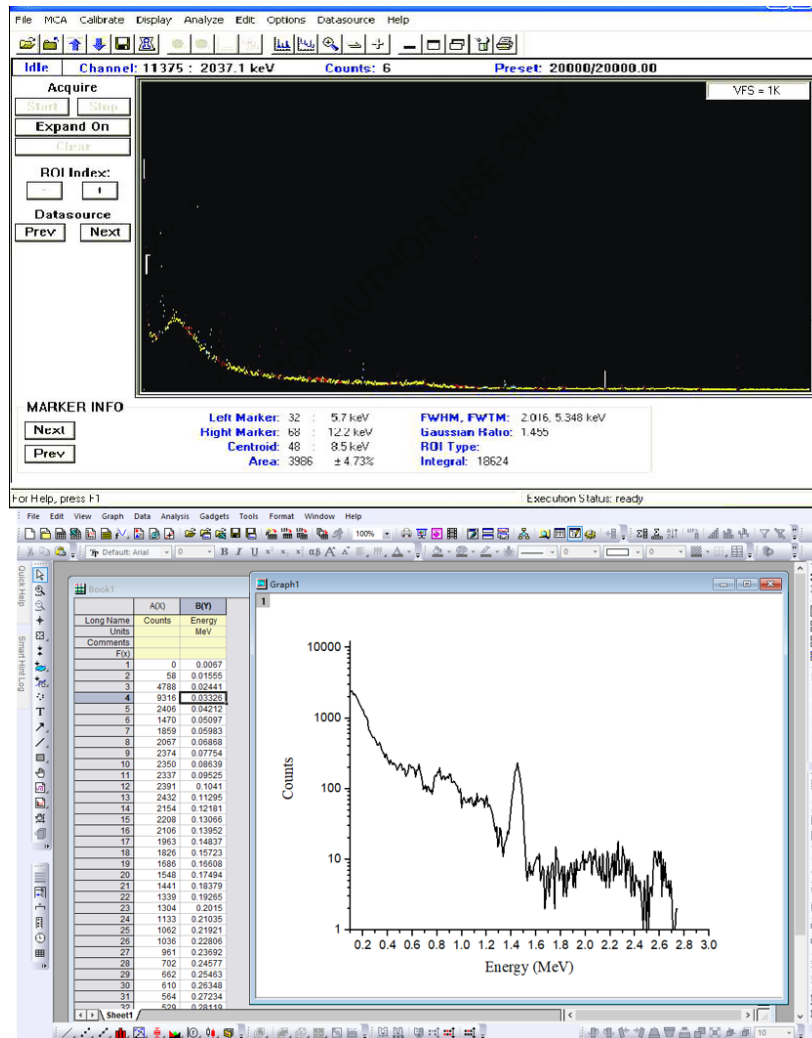


Figure 3.9: Gamma Acquisition & Analysis and OriginPro 9.1 interface [39].

3.3.3 Laboratory Description

The experiment was processed at the Energy Research Center (ERC) at Ontario Tech University in Oshawa, Canada. The neutron facility was constructed in a shielded room surrounded by control rooms and laboratories, housing auxiliary support equipment. The generator was placed at the center of a 775 x 775 cm square room, with a height of 400 cm in the basement of the ERC building. Three of the four sides of the room are composed of heavy concrete with a density of 3.8 g/cm³, with the last wall constructed from ordinary concrete with a density of 2.35 g/cm³ as there is ground soil behind it. All of the heavy concrete walls are 100 cm thick.

This neutron facility has a safety system to prevent personnel from being present during experiments to prevent them from being irradiated. This involves a locking system on the door, where the sources could only be activated when the door was closed. This door required an identification card along with a fingerprint scan to open. There was also a button on the wall inside the facility, which when pushed, turned an alarm on giving the operators 30 seconds to leave the room and close the door. When both were completed the operator was able to activate the neutron generator in the control room, and the experiment was completed.

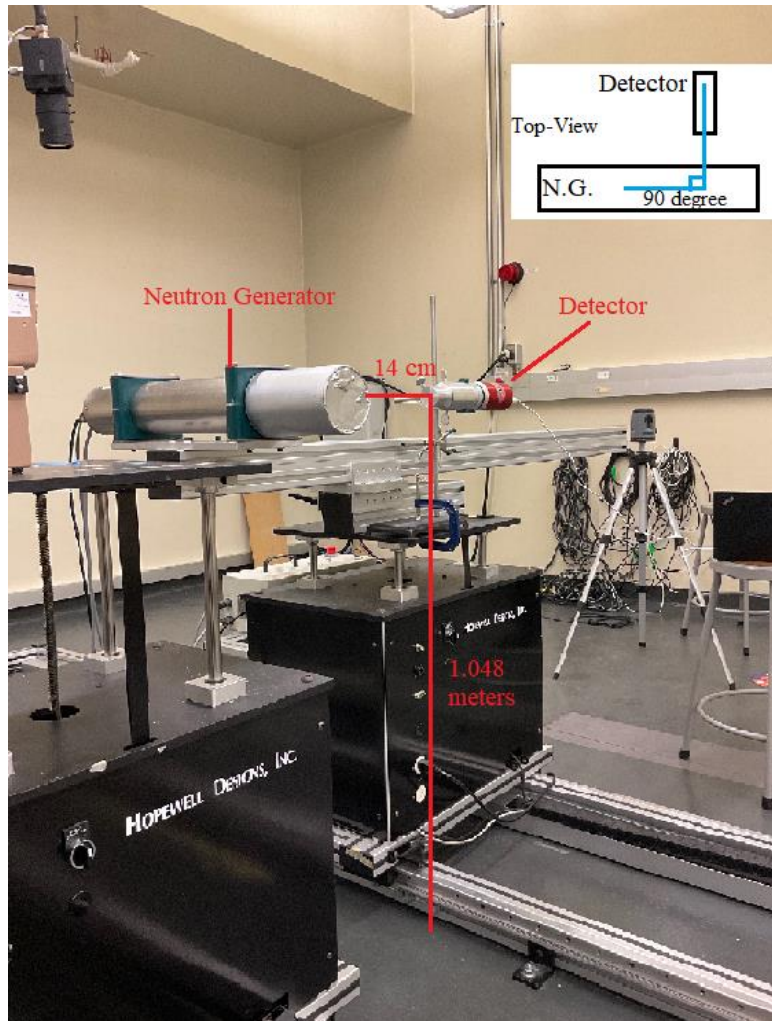
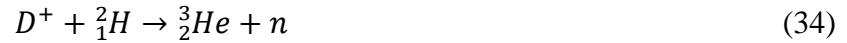


Figure 3.10: Experimental setup for neutron detection.

The experimental setup is shown in Figure 3.10, the neutron generator was placed horizontally in the middle of the neutron facility, the height was 1.048 meters from the center of the neutron generator tube to the ground. The LaCl_3 detector was placed at the same height, 90 degrees from the side of the neutron generator 14 cm away. The detector was set to a high voltage mode of 500 V, and both the gain value and the fine G value were set to 2.

3.3.4 Neutron Generator

The neutron generator used was a Thermo-Scientific P-385 D-D model that generates neutrons with an average energy of approximately 2.5 MeV and a neutron intensity of 10^6 neutrons per second using the reaction seen in Equation 34.



The (D, D) neutron generator produces neutrons when a deuterium beam is incident upon a metal hydride target, containing two deuterium atoms per metal atom. To produce a deuterium beam, the deuterium must have the electron removed in an ion-source in order to be able to be accelerated within an applied electric field of 120 kV. Once the ion interacts with the deuterium atom target, they fuse together to produce a helium-3 atom and emit a fast neutron with 2.5 MeV energy.

The neutron generator was installed along with a 10 Ci gamma irradiator in the neutron facility. The P-385 operates with a maximum voltage of 130 kV and a beam current between 20 to 70 μ A [3]. The emitted neutron energy depends on the energy of the accelerated deuterons and its emission angle with respect to the direction of deuteron's ion beam.

3.4 Experimental Procedure

There were seven runs using the LaCl_3 detector for the experiment. There was one run for background measurement, two runs using a gamma source for calibrating the detector and determining the resolution, and four runs to generate neutron spectra. The experimental setup for each measurement is listed in Table 3.1.

Table 3.1: Experimental setup information for the seven measurements.

Run #	Target	Measured Time (s)	Comment
001	-	600	Background
002	Na-22 + Cs-137 sources placed directly touched with the detector.	388	Calibration
003	Na-22 source placed directly touched with the detector.	134	Analyze Resolution
004	Neutron Generator at 90° , 2.5 MeV (see Figure 3.10)	725	Neutron Spectrum
005	Neutron Generator at 90° , 2.5 MeV (see Figure 3.10)	710	Neutron Spectrum
006	Neutron Generator at 90° , 2.5 MeV (see Figure 3.10)	1019	Neutron Spectrum
007	Neutron Generator at 90° , 2.5 MeV (see Figure 3.10)	1019	Neutron Spectrum

The first run's purpose was to measure the background radiation. The second run was completed to measure a spectrum of two gamma sources,. The next 4 runs were completed to generate 4 neutron source spectra.

3.4.1 Background and calibration adjustment

It was verified that there was no radiation from other sources located in the laboratory that could effect the measured spectra. Then, the detector was connected to the Gamma Acquisition & Analysis software on a laptop. The detector was then turned on through the software and left to run for a measured time of 600 seconds. Afterwards, the measured counts per channel data were saved through the software as an OriginPlot file. This was used to subtract the background counts from each of the subsequent runs, by subtracting the individual counts per channel. Since the background run's measured time was different from the other run's measured time, the counts needed to be adjusted based on the ratio of the measured time for each run with respect to the background's measured time.

Next, a calibration procedure was completed using the data from run 002, which included two gamma sources, ^{22}Na and ^{137}Cs . The procedure was much the same as the background procedure, but the two sources were placed on a table, and the detector placed on top directly touching the sources. This was used to generate a spectrum to find the peaks for the gamma sources. These peaks coordinates were used to generate a calibration graph with a regression model applied. This regression model resulted in a linear equation that was applied to the x-axis of the subsequent spectra, in order to convert the measured channel numbers to their gamma equivalent energy.

3.4.2 Neutron Detection Procedure

For the four runs using the neutron source, the neutron generator and detector was setup as shown in Figure 3.10. Next, the safety procedure was followed, and the operator turned on the

neutron detector and generator. The recorded spectra were compared with each other and with the MCNP results to verify that they were in agreement. These spectra were then analysed to verify if the LaCl_3 crystal material can be used as a suitable fast neutron scintillation detector.

3.5 References

3. Alberts, W.G., et al., *Development of electronic personal neutron dosimeters: a European cooperation* Radiation Protection Dosimetry, 2001. **96**(1-3): p. 251-254.
8. Bessiere, A., et al., *New thermal neutron scintillators: Cs/sub 2/LiYCl/sub 6/:Ce/sup 3+/
and Cs/sub 2/LiYBr/sub 6/:Ce/sup 3+/. IEEE Transactions on Nuclear Science, 2004. **51**(5):
p. 2970-2972.*
9. Bessiere, A., et al., *Luminescence and scintillation properties of CS₂LiYCl₆:Ce³⁺ for γ
and neutron detection.* Nuclear Instruments and Methods in Physics Research Section A:
Accelerators, Spectrometers, Detectors and Associated Equipment, 2005. **537**(1-2): p. 242-
246.
13. Machrafi, R., A.L. Miller, and K. N., *New approach to neutron spectrometry with multi
element scintillator.* Radiation Measurement, 2015. **80**(ELSEVIR Ltd.): p. 10-16.
35. et, J.K.T., *Nuclear Data Sheets.* National Nuclear Data Center.
36. Web, J., *Incident Neutron Data/ENDF/B-VII.1/C135/MT=103: (z,p)/Cross section.* 2022,
JANIS Web.
37. Laboratory, L.A.N., *Monte Carlo Methods, Codes, & Applications Group.* Los Alamos
National Laboratory.
38. EO, S., *LaCl₃(Ce) Scintillator Crystals.* 2022, Shalom EO.
39. Hossain, A., M.M. Rahman, and M. Kamal, *Assessment of Terrestrial Radionuclides in the
Northern part of Chittagong City Corporation, Chittagong, Bangladesh.* 2019, Research
Gate.

CHAPTER 4: RESULTS AND DISCUSSION

4.1 Background and Detector Calibration

4.1.1 Background Measurement

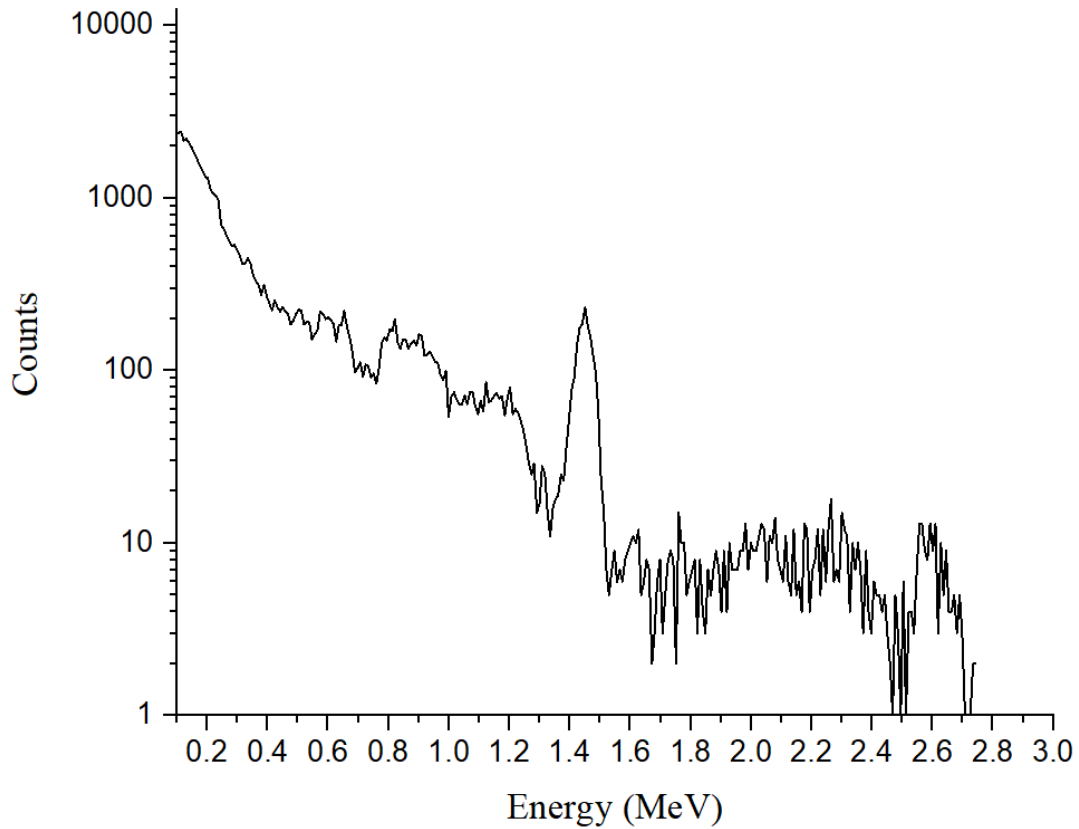


Figure 4.1: Background spectra.

Figure 4.1 presents the background measurement of the experimental environment for 10 minutes. This was used to discriminate the background noise from further experiment's data.

4.1.2 Detector Calibration

The detector was calibrated with two standard gamma sources i.e., ^{22}Na , ^{137}Cs , the information of the measured channels and counts corresponding to their actual energy for calibration are shown in Table 4.1. By using this information, a regression model and calibration equation were generated, shown in Figure 4.2.

Table 4.1: Calibration data of detector with ^{137}Cs and ^{22}Na from measured data.

	Channel	Counts	Energy (keV)
Na-22 ¹	59	22956	511
Cs-137	76	178959	661.66
Na-22 ²	145	1483	1274.53
Na-22 ¹⁺²	203	215	1785.53

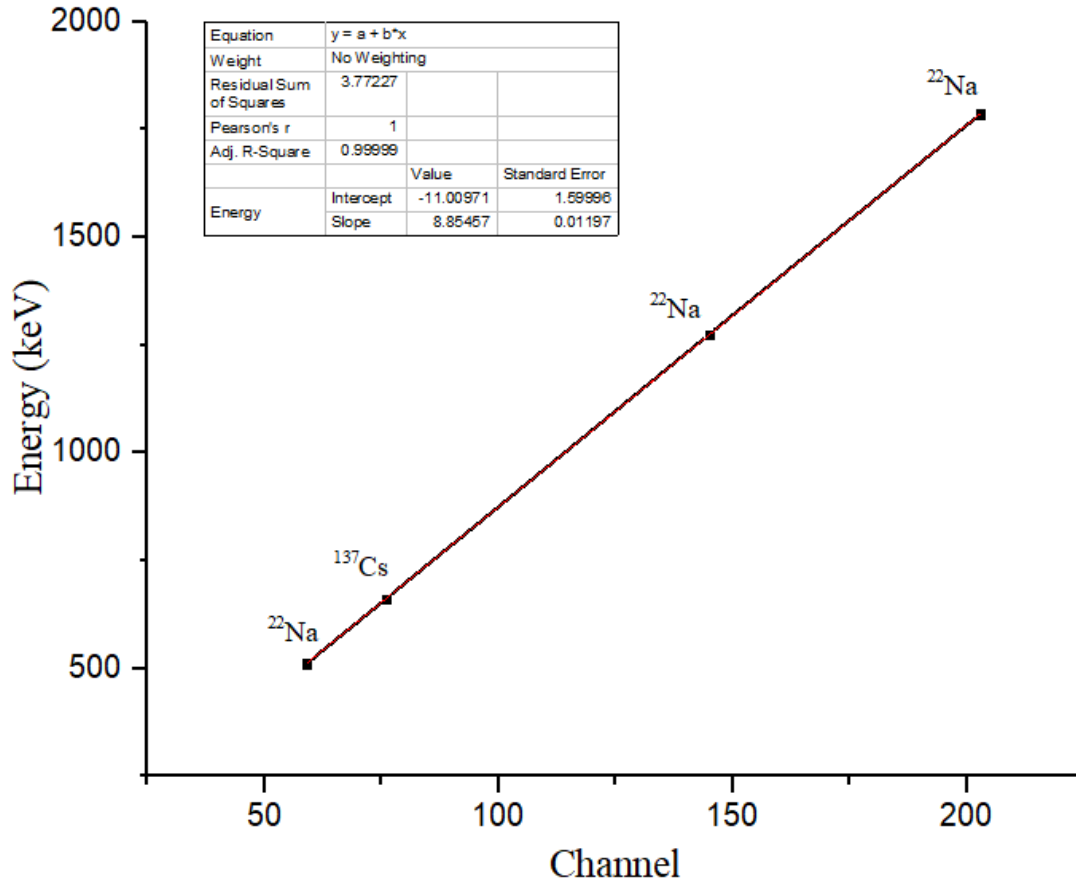


Figure 4.2: Calibration line of the detector with ^{137}Cs and ^{22}Na .

The calibration equation determined from Figure 4.2 can be seen in Equation 35.

$$y = 8.85457 * x - 11.00971 \quad (35)$$

With a coefficient of determination of,

$$R^2 = 0.9999$$

The y-axis is the corresponding peak energy in keV and x-axis is the peak channel number. By applying the calibration equation to the measured spectra of the calibration sources, ^{137}Cs and ^{22}Na , a new spectrum with counts over energy is generated, as seen in Figure 4.3.

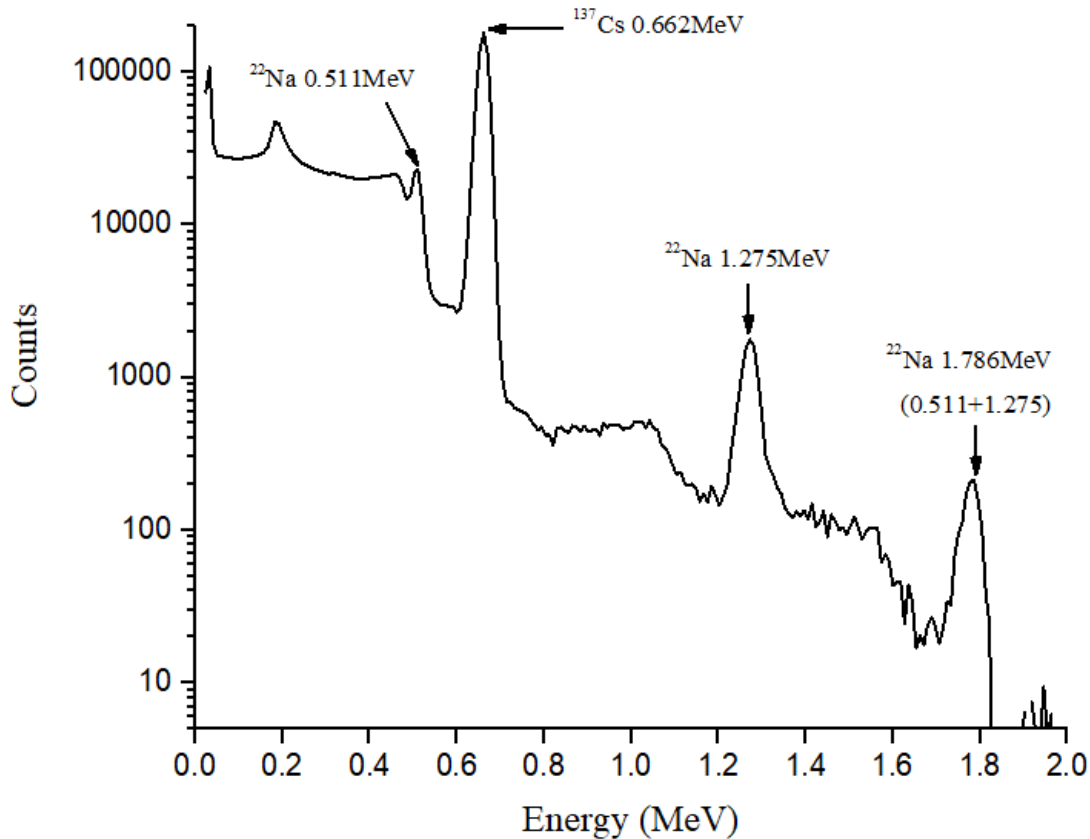


Figure 4.3: Calibrated response function of the $\text{LaCl}_3:\text{Ce}$ scintillator using ^{137}Cs and ^{22}Na gamma sources.

The spectrum displays three clear full energy deposition peaks corresponding to the sources' gamma rays. They are at the energies, 0.511 MeV, 0.662 MeV, and 1.275 MeV. There is also a double absorption peak at 1.786 MeV for the two gamma energies of the ^{22}Na source which were recorded by the detector at the same time. Therefore, the experiments using the neutron generator were calibrated with these gamma sources and the neutron energies were given in MeV, which represents the gamma equivalent energy. This unit represents the gamma energy that would correspond to the peak position observed for the protons and alpha particles interacting with the scintillating material.

4.2 Gamma Detection and Detector Resolution

This experiment used a ^{22}Na gamma source with the $\text{LaCl}_3:\text{Ce}$ detector for gamma radiation to measure the resolution of the detector to be used to model the experiment in MCNP/X.

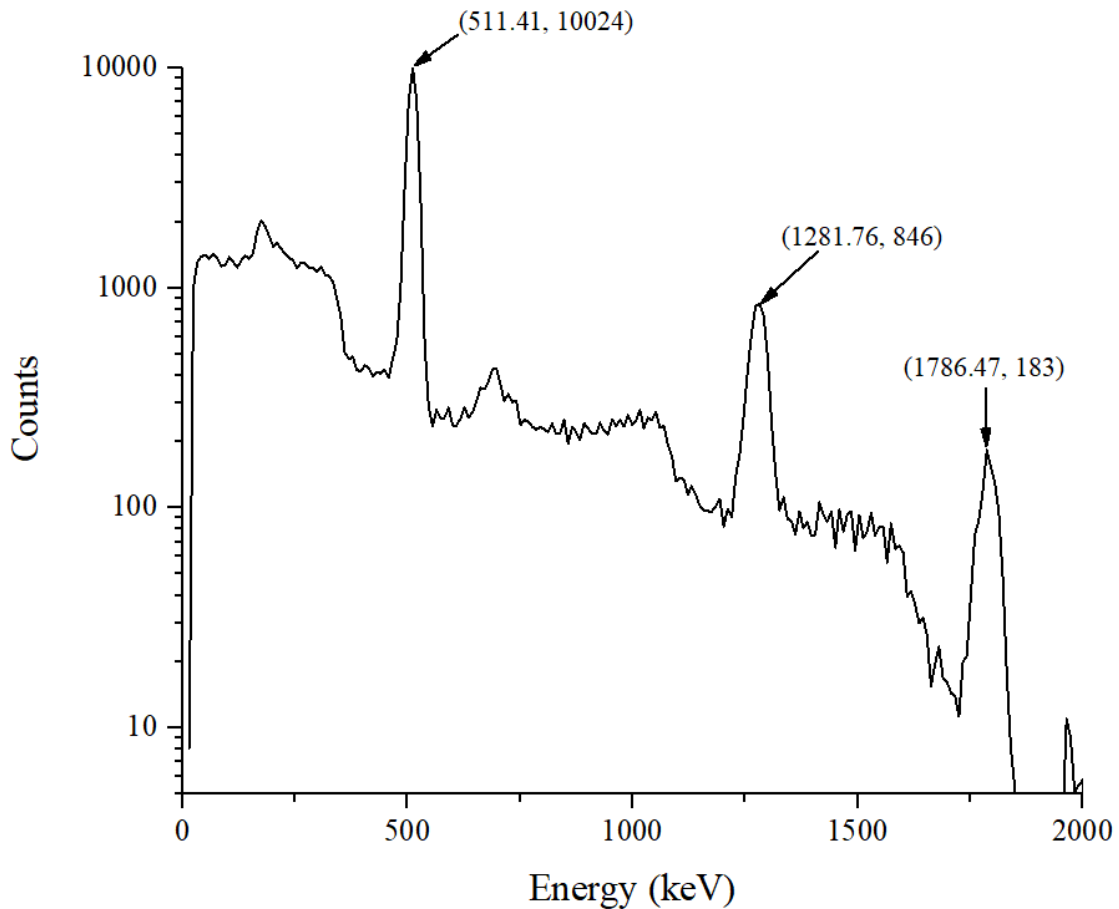


Figure 4.4: Measured pulse height spectrum of LaCl_3 using ^{22}Na gamma source.

As shown in Figure 4.4, using the peak at 511 keV, the coordinates of the FWHM on each side are (498.21, 5012) and (524.40, 5012). The resolution of the LaCl_3 detector at 511 keV for ^{22}Na was calculated using Equation 23 as follows in Equation 36,

$$R = \frac{(524.40-498.21)}{511.41} * 100\% = 5.12\% \approx 5\% \quad (36)$$

The equation to calculate the GEB function that will be used within the MCNP/X code is shown in Equation 37. This equation is used to adjust and convert the initial unbroadened energy of the particles to the broadened energies.

$$f(E) = C * e^{-\left(\frac{E-E_0}{A}\right)^2} \quad (37)$$

In which,

E is the broadened energy, MeV

E₀ is the unbroadened energy of tally, MeV

C is the normalization constant

A is the Gaussian width, MeV

The Gaussian width, A, is calculated using Equation 38.

$$A = \frac{FWHM}{2*\sqrt{\ln 2}} \quad (38)$$

In which,

A is the Gaussian width, MeV

In the MCNP/X code the constant for the FWHM can be calculated using Equation 39.

$$FWHM = a + b * \sqrt{E} + c * E^2 \quad (39)$$

In which,

a is a constant, MeV

b is a constant, MeV^{1/2}

c is a constant, MeV⁻¹

E is the particle energy, MeV

By using the measured ²²Na pulse height spectrum in Figure 4.4, the FWHM values were calculated and shown in Table 4.2.

Table 4.2: Coordinates for FWHM calculations and FWHM values.

Centroid Peak	FWHM on Left	FWHM on Right	FWHM values (keV)
(511.41, 10024)	(498.21, 5011.82)	(524.40, 5011.82)	26.20
(1281.76, 846)	(1255.15, 422.76)	(1302.10, 422.76)	46.95
(1786.47, 183)	(1769.74, 91.44)	(1813.57, 91.44)	43.82

Therefore, by using the centroid peak energies of 0.511, 1.281, and 1.786 MeV and FWHM values of 0.0262, 0.04695, and 0.04382 MeV, the constants a, b, and c can be calculated by solving a system of equations generated by Equation 39;

$$a = -5.46497 * 10^{-2} \text{ MeV},$$

$$b = 1.21336 * 10^{-1} \text{ MeV}^{\frac{1}{2}},$$

$$c = -3.5339 * 10^{-1} \text{ MeV}^{-1}.$$

When the constants were calculated, a function of FWHMs corresponding to particle energies can be established from Equation 39, and the Gaussian width, A, can be calculated using the Equation 38. Therefore, the MCNP/X now has the ability to calculate the broadened energy from the initial unbroadened energy in Equation 37.

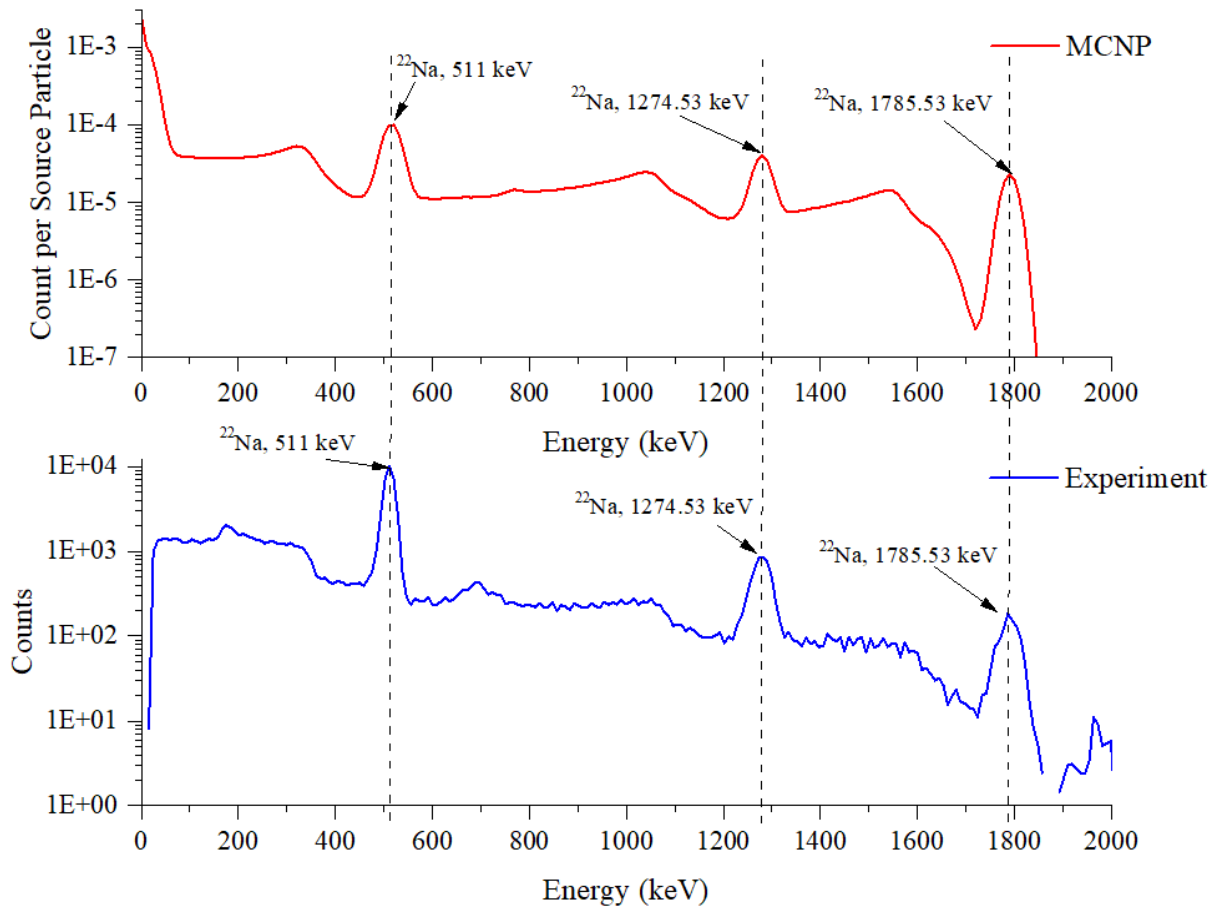


Figure 4.5: Pulse height spectrum of LaCl₃ using ²²Na gamma source.

In figure 4.5, a comparison of the results between the MCNP/X simulation and experimental measurements using a ²²Na gamma source is shown. The MCNP/X simulation

consisted of a ^{22}Na point source, and used the F8 tally in order to simulate a physical LaCl_3 detector. This simulation was allowed to run for 120 minutes with 2.131×10^9 source particles. The result of the MCNP simulation displays three energy peaks similar to the experimental results, along with similar trends. The discrepancy between the two spectra is minimal, and is the result of MCNP not being capable of simulating background radiation.

4.3 MCNP Simulation Results

The simulated spectra using MCNP for the, $^{35}\text{Cl}(n, p)$, $^{35}\text{Cl}(n, \alpha)$, and neutron-gamma reactions for different particles are presented below from Figure 4.6 to Figure 4.10. The $^{35}\text{Cl}(n, p)$ reaction from 2.5 MeV incident neutrons are expected to have four theoretical energy levels at 3.11, 1.54, 1.12, and 0.76 MeV, which corresponds to the ground state, 1st, 2nd, and 3rd excited states, respectively.

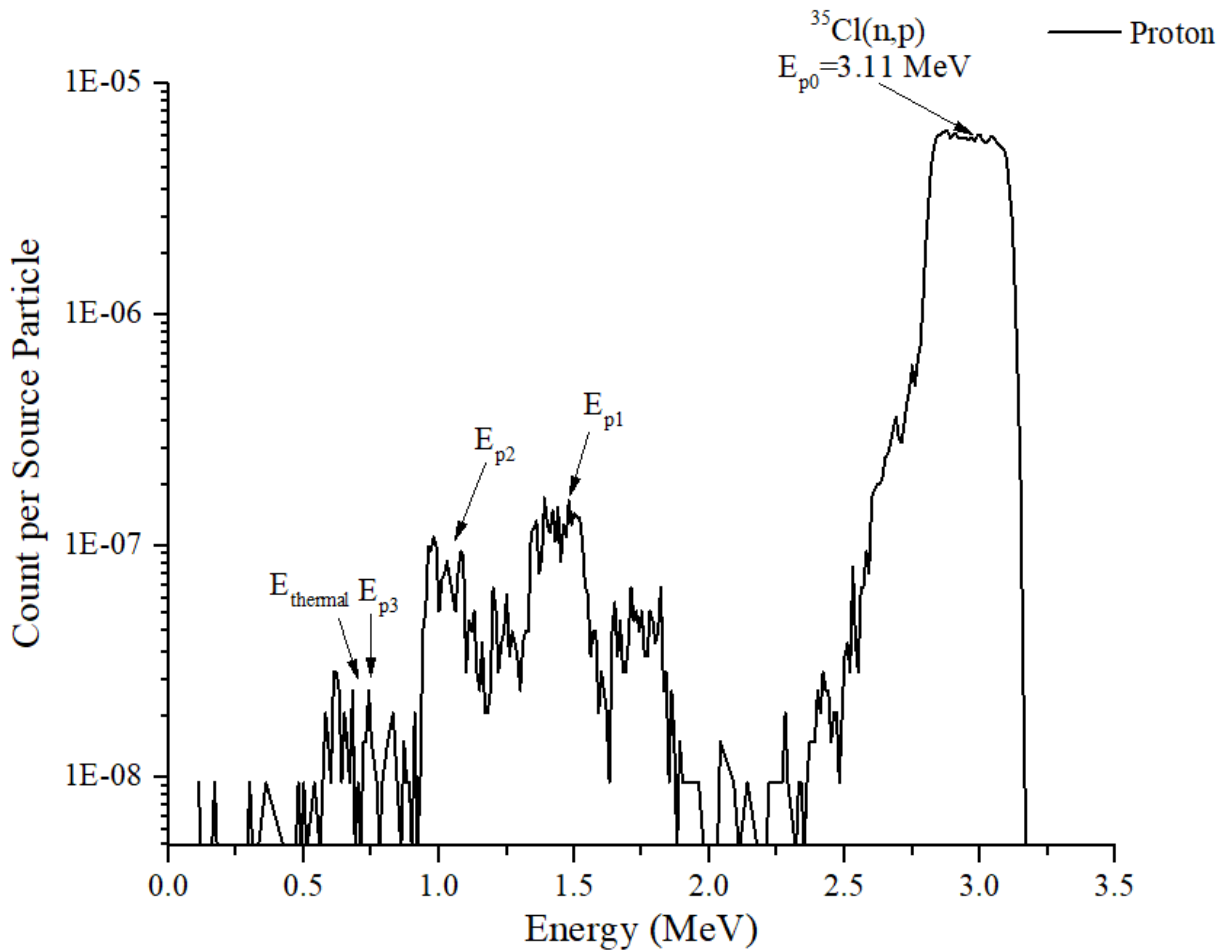


Figure 4.6: $^{35}\text{Cl}(n, p)$ response function of the LaCl_3 detector to 2.5 MeV neutrons with only protons tallied.

The simulated response function for protons in Figure 4.6 observed a prominent continuum peak, E_{p0} , located around 3.11 MeV energy, this energy corresponds to the protons emitted from the $^{35}\text{Cl}(n, p)$ reaction at $Q + 2.5$ MeV (E_n), when the produced sulfurs are in ground state. There are two major secondary peaks below the prominent peak, which can also be clearly observed from the spectrum, E_{p1} and E_{p2} . These two peaks are located around 1.5 MeV and 1 MeV respectively, which match the theoretical energy levels of the $^{35}\text{Cl}(n, p)$ reactions at the 1st and 2nd excited states of the recoiled sulfurs. Furthermore, there are some noticeable peaks appearing in the energy range between 0.5 to 0.75 MeV where the expected peaks of the thermal neutrons (0.615 MeV) and 3rd excited state of recoiled sulfurs (0.76 MeV) should be located.

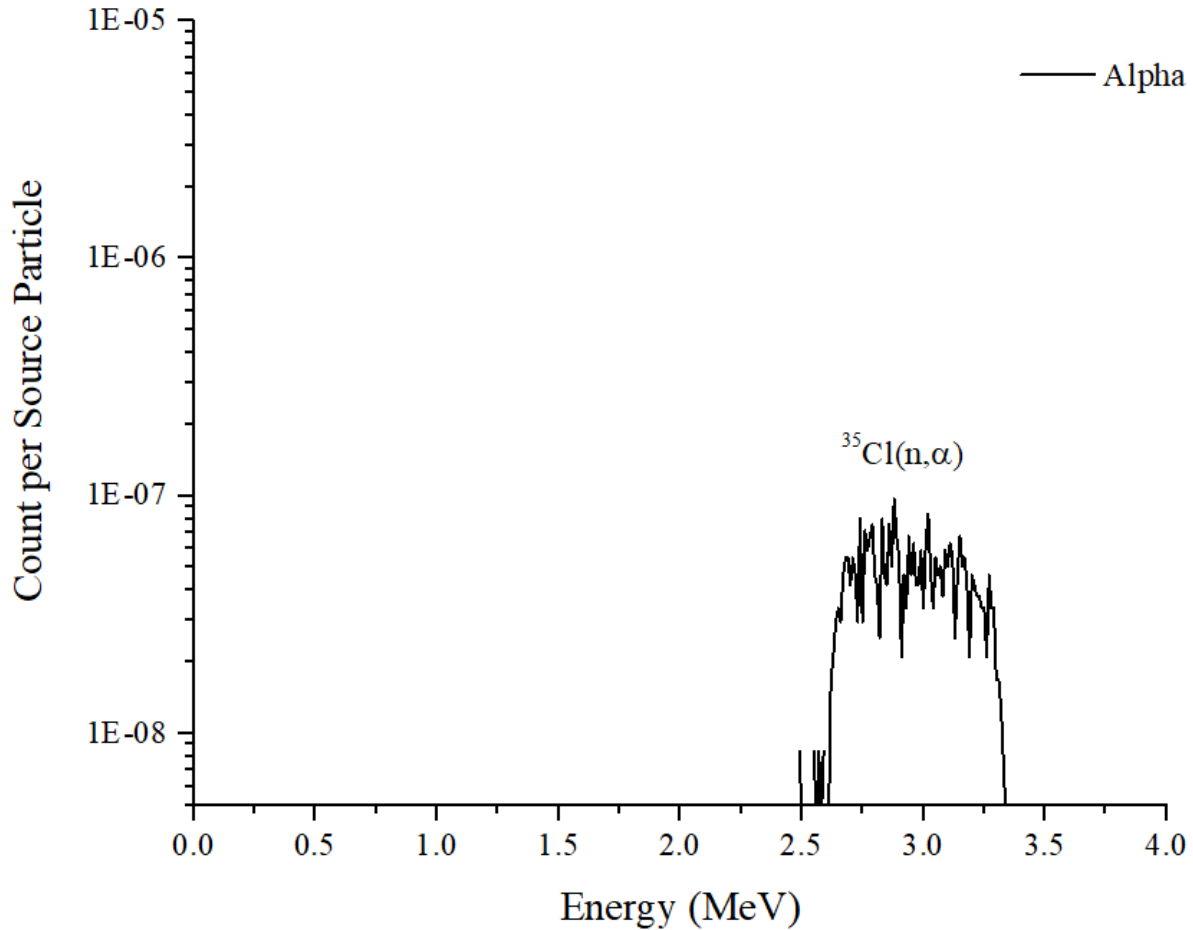


Figure 4.7: $^{35}\text{Cl}(n, \alpha)$ response function of the LaCl_3 detector to 2.5 MeV neutrons with only alpha particles tallied.

The simulated response function shown in Figure 4.7 displays the results of the $^{35}\text{Cl}(n, \alpha)$ reaction when only alpha particles are tallied. A continuum peak is observed in the energy range between 2.6 to 3.3 MeV. According to the ^{35}Cl neutron cross-section in Figure 3.5, this continuum peak can be identified as the peak resulting from $^{35}\text{Cl}(n, \alpha)^{32}\text{P}$ reactions. The peaks on the spectrum appear as a continuum instead of distinguishable peaks due to the similar energy levels of ^{32}P .

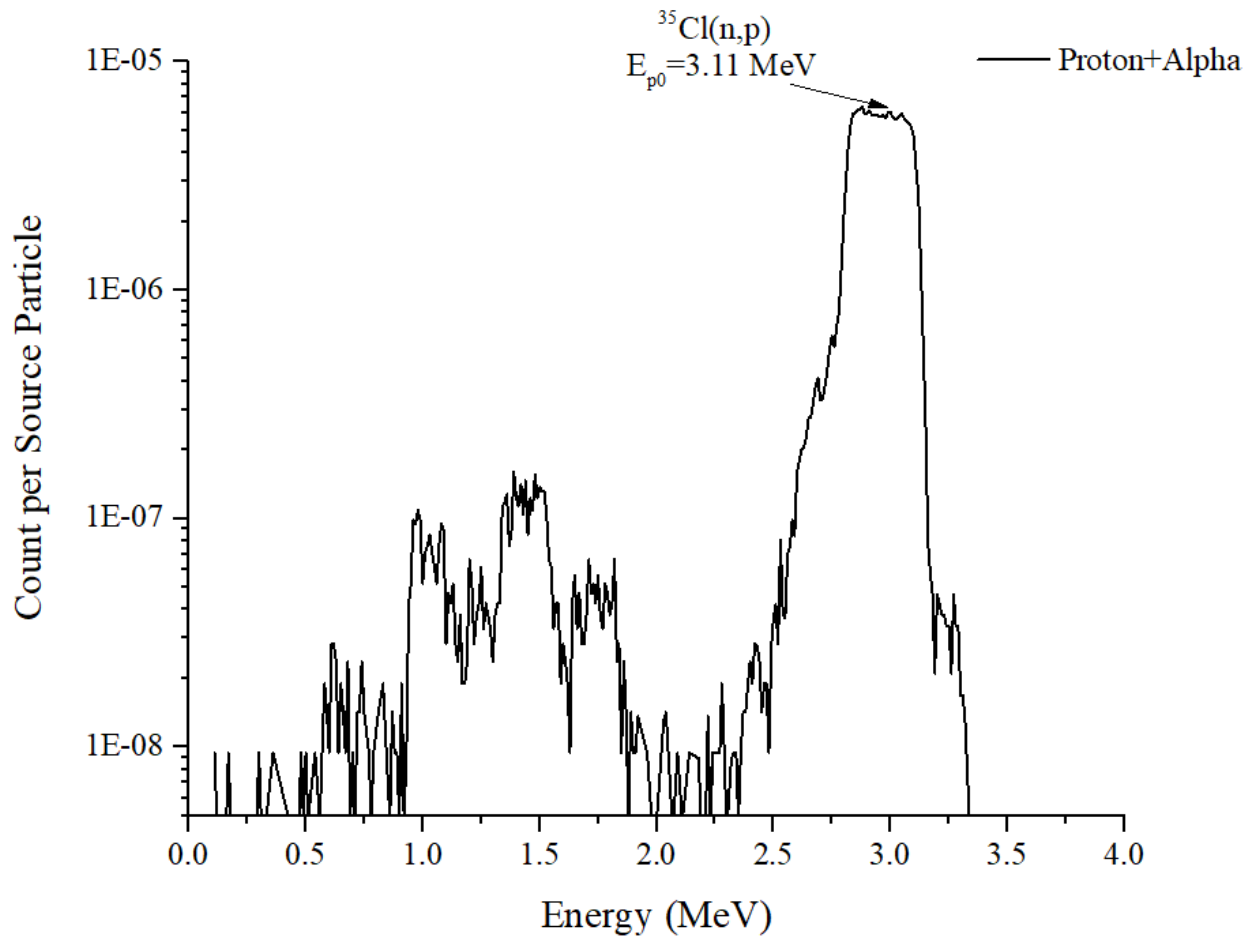


Figure 4.8: $^{35}\text{Cl}(n, \alpha)$ and $^{35}\text{Cl}(n, p)$ response function of the LaCl_3 detector to 2.5 MeV neutrons with protons and alpha particles tallied together.

The simulated response function in Figure 4.8 displays the results when protons and alpha particles are tallied together within MCNP/X. Since the pulse height counts for the $^{35}\text{Cl}(n, \alpha)$ reactions are significantly lower than the counts of the $^{35}\text{Cl}(n, p)$ reaction, the spectrum does not show a significant change compared with the proton only spectrum. The only changes prevalent is a broadening of the prominent peak.

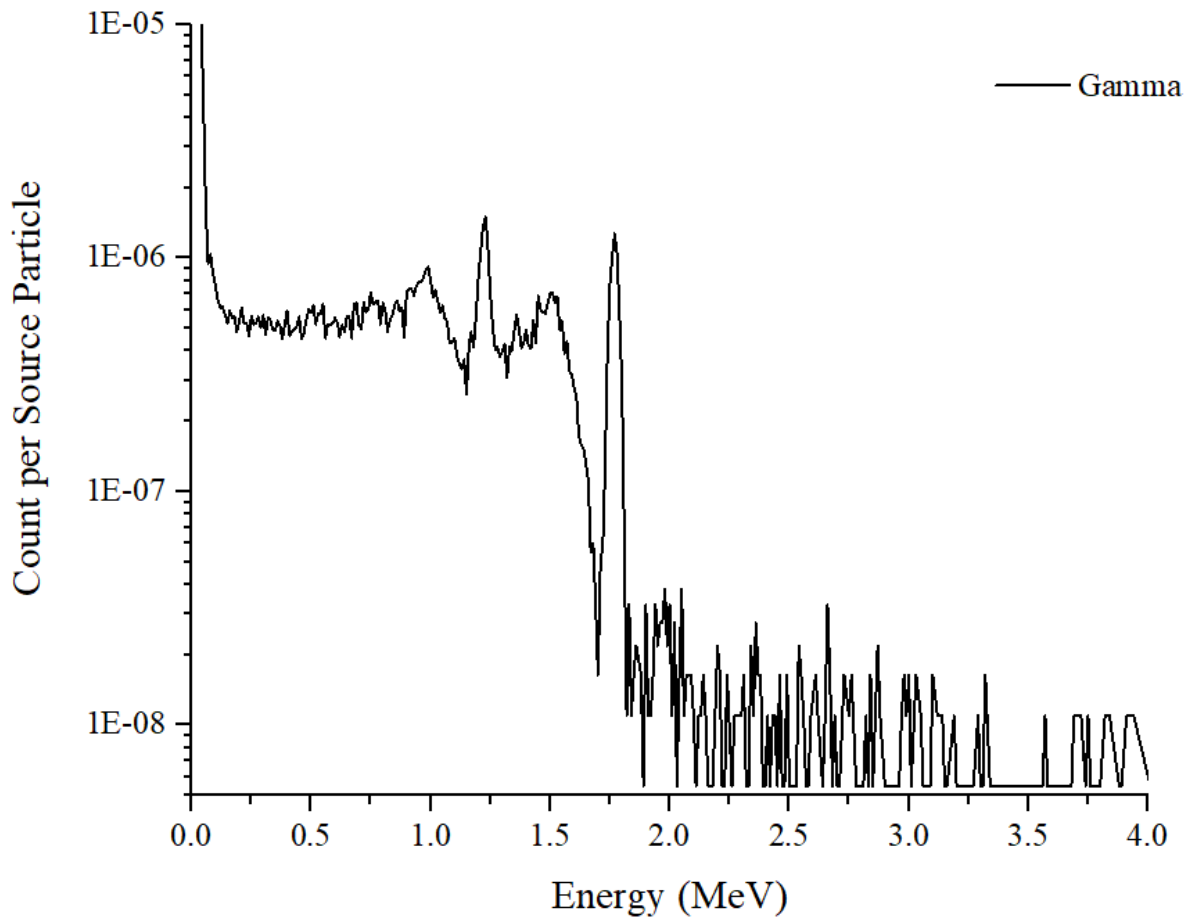


Figure 4.9: $^{35}\text{Cl}(n, \alpha)$ and $^{35}\text{Cl}(n, p)$ response function of the LaCl_3 detector to 2.5 MeV neutrons with only gammas tallied.

The simulated response function in Figure 4.9 displays the resonance gamma radiation emitted after the $^{35}\text{Cl}(n, \alpha)$ and $^{35}\text{Cl}(n, p)$ reactions if the produced atoms are excited. This spectrum is used to verify that the resonance gamma radiation produced does not coincide with the prominent peak energy from $^{35}\text{Cl}(n, p)$ reactions.

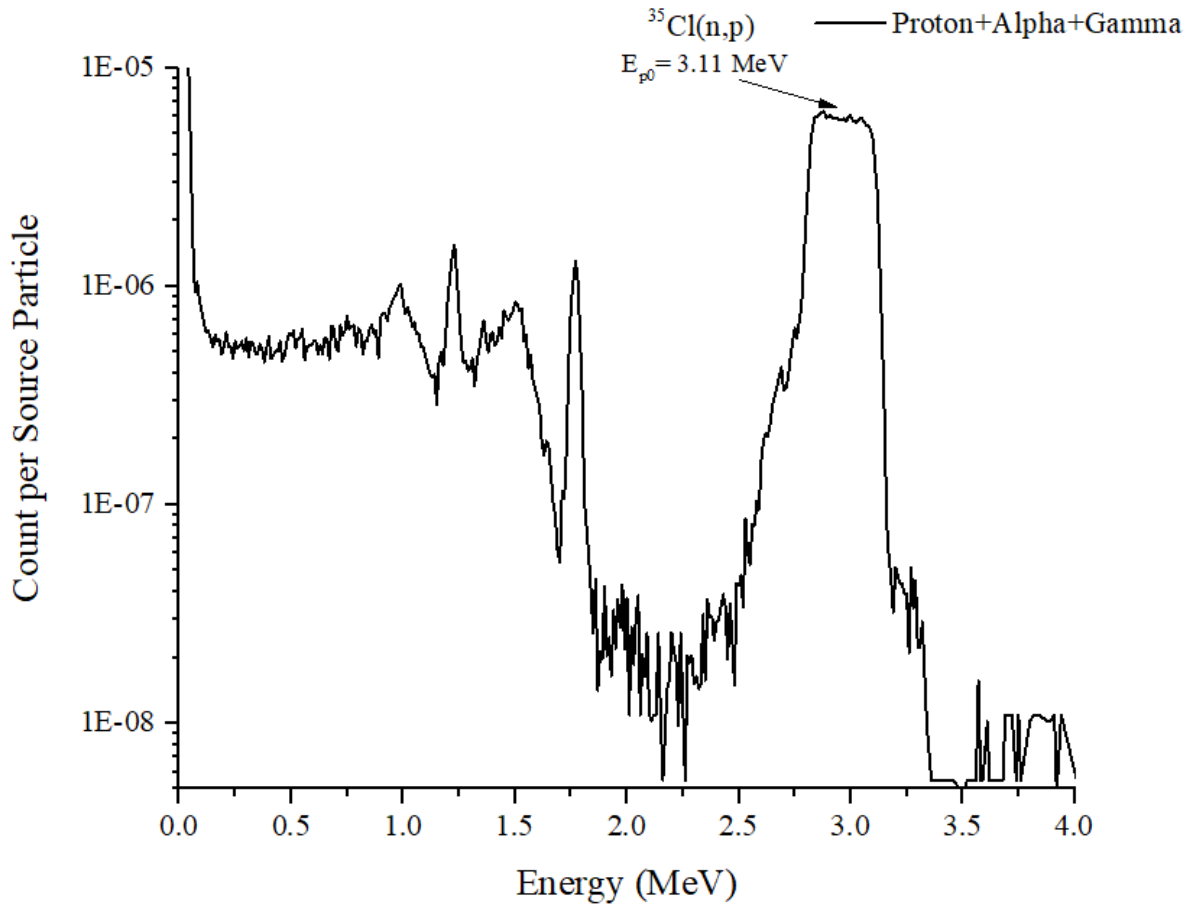


Figure 4.10: $^{35}\text{Cl}(n, \alpha)$ and $^{35}\text{Cl}(n, p)$ response function of the LaCl_3 detector to 2.5 MeV neutrons with protons, gammas, and alpha particles tallied.

As seen in Figure 4.10, a spectrum was generated to include protons, gammas, and alpha particles that are emitted through the neutron induced ^{35}Cl reactions. Through analysis of the spectrum, it becomes apparent that the gamma radiation is only prevalent at lower energies ($E_\gamma < 1.75$ MeV), therefore it does not coincide with the prominent peak of the $^{35}\text{Cl}(n, p)$ reaction. As a result, it becomes easier to discriminate between the photons generated through the protons and alphas interacting with the scintillating material, and the photons directly generated through the ^{35}Cl reactions. This response function will be used to verify with the spectra measured in section 3.4.

4.4 Experimental Results

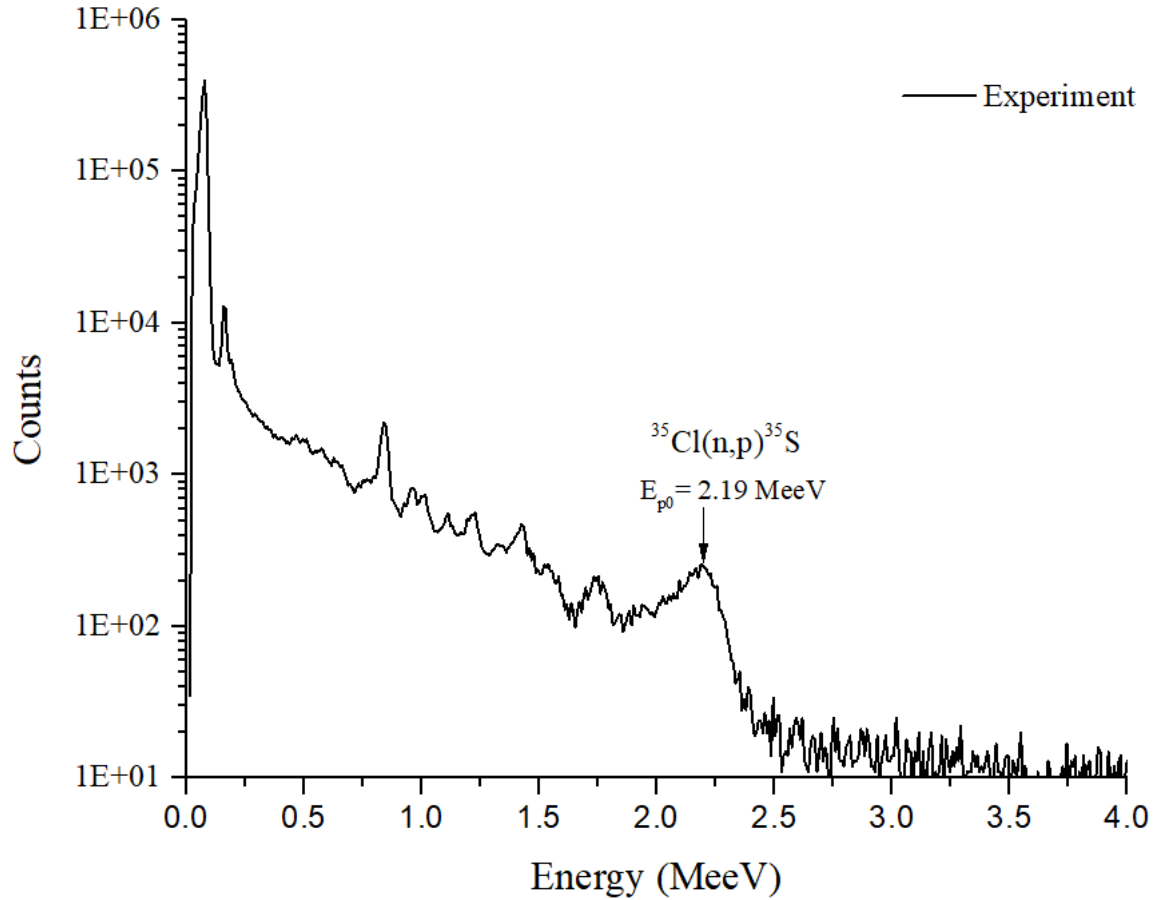


Figure 4.11: Measured response function of the LaCl₃:Ce scintillator with 2.5 MeV neutrons.

Figure 4.11 presents the measured response function of the LaCl₃ scintillator with mono-energetic incident neutrons of 2.5 MeV. The spectrum observed a prominent peak at 2.19 MeeV, which represents the main proton induced photon peak of the ³⁵Cl (n, p) reaction. However, the theoretical position of the prominent peak should be at 3.11 MeV. The resolution of this prominent neutron peak was calculated to be 12.11%.

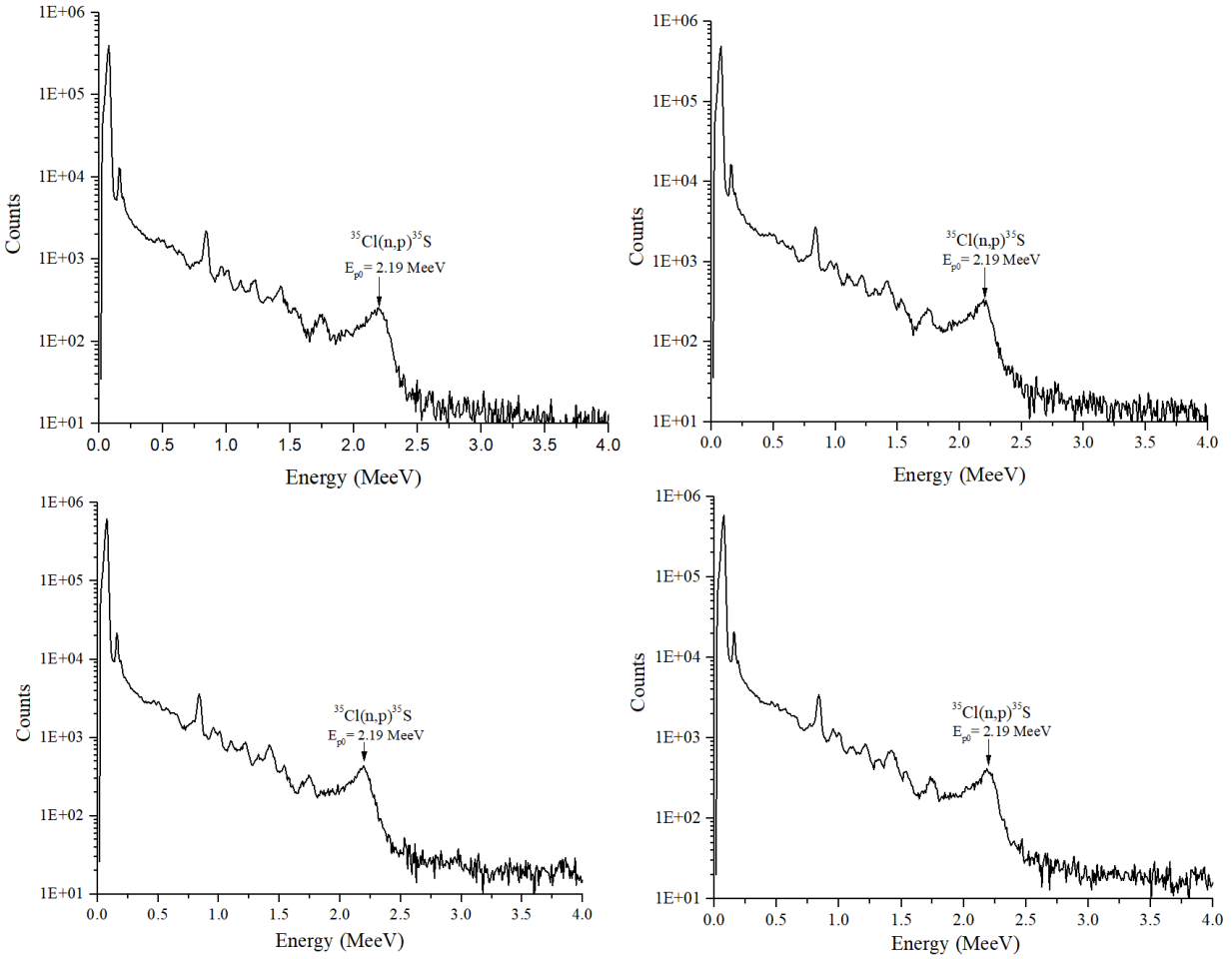


Figure 4.12: Comparison of measured response functions for each run.

The experiment was repeated 4 times to ensure the results were accurate. All four measured response functions for Run 004 to Run 007 are shown in Figure 4.12. These four measurements gave the same results displaying the prominent peak at 2.19 MeeV. To identify the peaks for the measured response function, a comparison with the simulation is needed.

4.5 Comparison

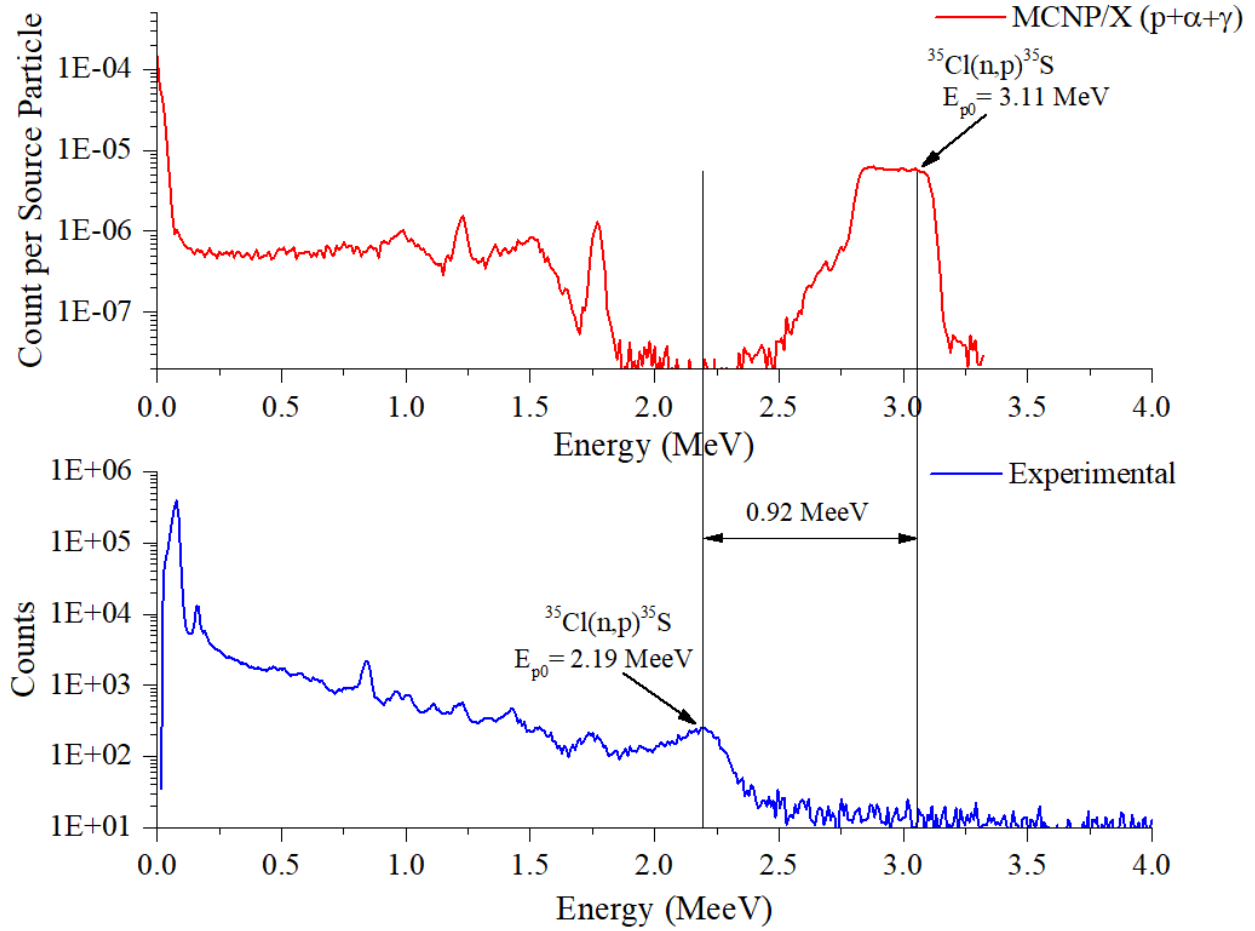


Figure 4.13: Comparison of the simulated and measured response function of LaCl_3 with 2.5 MeV mono-energetic neutrons.

For the purpose of comparing the two results, the units for the simulated and experimental results will be MeV and MeeV respectively. Figure 4.13 displays a comparison of the simulated and measured response functions of the LaCl_3 detector with 2.5 MeV incident neutrons. A displacement of the prominent peak is observed in the experimental spectrum with respect to the simulated spectrum. This lowers the simulated peak's energy of 3.11 MeV by 0.92 MeeV, which results in an experimental peak energy of 2.19 MeeV. This reduction of energy is caused by quenching. As mentioned in section 3.3.1 regarding LaCl_3 crystal scintillates, the energy from the

incident neutron is converted to visible light (photons) in order to be processed in the PMT, however the quenching can cause an energy shift in a peak. This quenching can be the result of two different reasons. The first reason is the result of the LaCl_3 molecules becoming saturated, whereas, the molecule is already excited and cannot produce further photons. This happens once the energy of the recoil protons undergo alternate de-excitation modes which are radiationless, such as heat, which caused no photons to be emitted from the scintillator. The next reason is the result of the crystal not being perfectly clear causing the photons to be absorbed by the color of the crystal, though this is not attributed to much of the quenching in this case as the crystal was relatively colorless. In order to correct peak's energy, it is necessary to repeat the experiment at multiple incident fast neutron energy levels to calibrate the detector, which would also convert the x-axis from MeV to MeV.

CHAPTER 5: CONCLUSION

This thesis investigated a $\text{LaCl}_3\text{:Ce}$ scintillator for fast neutron spectrometry. The scintillator was installed on a PMT coupled with a MDA system for a series of experiments to determine the response functions for gamma rays and fast neutrons. To verify the measured response functions were reliable, MCNP/X code was used to simulate the experiment with similar geometry as the experimental room using a F8 tally to track the emitted particles from the reaction.

In the first gamma ray detection experiment, the scintillator was irradiated with a ^{22}Na gamma source. The pulse height spectra showed three significant peaks at 0.511 MeV, 1.275 MeV, and 1.786 MeV with the energy resolution calculated to be approximately 5%. The three energy peaks found in the experimental spectrum matched with the simulation results from MCNP/X verifying that the detector worked as intended.

After the gamma experiment, the scintillator was irradiated with a neutron generator with mono-energetic fast neutrons of 2.5 MeV energy. The gamma equivalent energy of the prominent proton peak was 2.19 MeV, this peak is the result of the $^{35}\text{Cl}(n, p)^{35}\text{S}$ reactions with the recoiled sulfurs left in ground state. This experiment was also simulated using MCNP/X models to tally protons, alpha particles, and gamma rays. The simulated spectra displayed a prominent peak at a theoretical energy of 3.11 MeV, which compared to the measured spectra, displayed a difference of 0.92 MeV between the peaks. This is a result of the radiation experiencing quenching, which lowered the counts and energy of the charged particles.

The detector was able to sufficiently measure fast neutrons above 1 MeV with the ability to discriminate between gamma radiation and the neutron induced proton and alpha radiation. The

detector had a resolution of 12.11% for $^{35}\text{Cl}(n, p)$ reactions, which is the dominant reaction when detecting the neutrons within this detector.

One application of LaCl_3 detector would use its ability to serve as a neutron monitor to measure neutron counts as well as the neutron energy in a (D, D) fusion system with neutron energy of 2.5 MeV. Since the $^{35}\text{Cl}(n, p)$ reaction also has the cross-section about 0.1 barn at 14 MeV, it can ideally be used as a monitor in a (D, T) fusion system with the neutron energy of 14 MeV. However, this ability needs to be experimentally proved as a part of the future works.

CHAPTER 6: FUTURE WORK

The approach presented in this master thesis had further supported the use of $\text{LaCl}_3:\text{Ce}$ scintillator to monitor fast neutrons produced in fusion systems. However, since this experiment only used a neutron generator with a fast neutron energy of 2.5 MeV, the proton quenching factor cannot be found, therefore, making it impossible to calibrate the measured curve and convert the measured protons response function from MeV to MeV. In future reports, multiple fast neutron sources will be used in order to calibrate the peak.

BIBLIOGRAPHY

- [1] W. G. Alberts, P. Alexandre, E. Arend, F. d'Errico, A. Fiechtner, H. Roos, H. Schuhmacher, C. Wernli and S. Wimmer, "Development of electronic personal neutron dosimeters: a European cooperation," *Radiation Protection Dosimetry*, vol. 96, no. 1-3, pp. 251-254, 2001.
- [2] R. Schutz, G. Fehrenbacher, M. Wielunski and W. Wahl, "A Three Si Detector System For Personnel Neutron Dosimetry Developed By Means Of Monte Carlo Simulation Calculations," *Radiation Protection Dosimetry*, vol. 104, no. 1, pp. 17-26, 2003.
- [3] J. Barthe, J. M. Bordy and T. Lahaye, "Electronic Neutron Dosimeters: History and State of the Art," *Radiation Protection Dosimetry*, vol. 70, no. 1-4, pp. 59-66, 1997.
- [4] C. M. Combes, P. Dorenbos, C. W. van Eijk, K. W. Kramer and H. U. Gudel, "Optical and scintillation properties of pure and Ce³⁺-doped Cs₂LiYCl₆ and Li₃YCl₆:Ce³⁺ crystals," *Journal of Luminescence*, vol. 82, no. 4, pp. 299-305, 1999.
- [5] A. Bessiere, P. Dorenbos, C. W. van Eijk, K. W. Kramer and H. U. Gudel, "New thermal neutron scintillators: Cs₂/LiYCl₆:Ce³⁺ and Cs₂/LiYBr₆:Ce³⁺," *IEEE Transactions on Nuclear Science*, vol. 51, no. 5, pp. 2970-2972, 2004.
- [6] A. Bessiere, P. Dorenbos, C. W. van Eijk, K. W. Kramer and H. U. Gudel, "Luminescence and scintillation properties of CS₂LiYCl₆:Ce³⁺ for γ and neutron detection," *Nuclear*

Instruments and Methods in Physics Research Section A: Accelerators, Spectrometers, Detectors and Associated Equipment, vol. 537, no. 1-2, pp. 242-246, 2005.

- [7] J. Glodo, W. M. Higgins, E. V. D. Van Loef and K. S. Shah, "Scintillation Properties of 1 Inch Cs₂LiYCl₆:Ce Crystals," *IEEE Transactions on Nuclear Science*, vol. 55, no. 3, pp. 1206-1209, 2008.
- [8] W. M. Higgins, J. Glodo, U. Shirwadkar, A. Churilov, E. Van Loef, R. Hawrami, G. Ciampi, C. Hines and K. S. Shah, "Bridgman growth of Cs₂LiYCl₆:Ce and ⁶Li-enriched Cs₂₆LiYCl₆:Ce crystals for high resolution gamma ray and neutron spectrometers," *Journal of Crystal Growth*, vol. 312, no. 8, pp. 1216-1220, 2010.
- [9] J. Glodo, E. van Loef, R. Hawrami, W. M. Higgins, A. Churilov, U. Shirwadkar and K. S. Shah, "Selected Properties of Cs₂LiYCl₆, Cs₂LiLaCl₆, and Cs₂LiLaBr₆ Scintillators," *IEEE Transactions on Nuclear Science*, vol. 58, no. 1, pp. 333-338, 2011.
- [10] D. T. Bartlett, R. J. Tanner and D. J. Thomas, "Active Neutron Personal Dosimeters – A Review of Current Status," *Radiation Protection Dosimetry*, vol. 86, no. 2, pp. 107-122, 1999.
- [11] J. Magill and J. Galy, "1. Origins and Discovery: The Neutron," in *Radioactivity Radionuclides Radiation*, Berlin, Springer, 2005, pp. 11-12.
- [12] R. Machrafi, "Neutron Interaction with Matter," Ontario Tech University, Oshawa, 2018.

- [13] IAEA Nuclear Data Section, "Parent Daughter Chain," IAEA, 2021. [Online]. Available: <https://nds.iaea.org/relnsd/vcharthtml/decaychain.html#NUCID=252CF>. [Accessed 29 December 2021].
- [14] Frontier Technology Corporation, "Californium-252 (Cf-252) Production," Frontier Technology Corporation, [Online]. Available: <https://www.frontier-cf252.com/californium-information/production/>. [Accessed 29 December 2021].
- [15] R. Machrafi, "RADI4430U-Industrial Application of Radiation Techniques Lab Manual," Ontario Tech University, Oshawa, 2019.
- [16] G. Knoll, "Neutron Sources," in *Radiation Detection and Measurement, 2nd ed*, United States, John Wiley and Sons Inc., 1989, pp. 20-28.
- [17] Phoenix, "D-D neutron Generator (Deuterium-Deuterium)," Phoenix, 26 January 2021. [Online]. Available: <https://phoenixwi.com/neutron-generators/dd-deuterium-deuterium-neutron-generators/>. [Accessed 30 December 2021].
- [18] S. N. Ahmed, "General Properties and Sources of Particles and Waves," in *Physics and Engineering of Radiation Detection*, AMSTERDAM, BOSTON, HEIDELBERG, LONDON, NEW YORK, OXFORD, PARIS, SAN DIEGO, SAN FRANCISCO, SINGAPORE, SYDNEY, TOKYO, ELSEVIER, 2015, p. 51.
- [19] G. Knoll, "Interaction of Neutrons," in *Radiation Detection and Measurement, 2nd*, United States, John Wiely and Sons Inc., 1989, pp. 57-59.

- [20] S. N. Ahmed, "2.6 Interaction of Neutral Particles with Matter," in *Physics and Engineering of Radiation Detection*, AMSTERDAM, BOSTON, HEIDELBERG, LONDON, NEW YORK, OXFORD, PARIS, SAN DIEGO, SAN FRANCISCO, SINGAPORE, SYDNEY, TOKYO, John Wiley and Sons Inc., 1989, pp. 137-140.
- [21] A. Marks, ANSTO, A. Reynolds, A. Nero, C. Hill and R. Pease, "Physics of Uranium and Nuclear Energy," World Nuclear Association, November 2020. [Online]. Available: <https://world-nuclear.org/information-library/nuclear-fuel-cycle/introduction/physics-of-nuclear-energy.aspx>. [Accessed 30 December 2021].
- [22] T. W. Kerlin and B. R. Upadhyaya, "7.3 Moderator temperature feedback in thermal reactors," in *Dynamic and Control of Nuclear Reactor*, Londo, San Diego, Cambridge, Oxford, Elsevier Science & Technology, 2019, p. 76.
- [23] R. Machrafi, "Fundamentals of Radiation Detectors," Ontario Tech University, Oshawa, 2019.
- [24] G. Knoll, "General Properties of Radiation Detectors," in *Radiation Detector and Measurement, 2nd ed*, United States, John Wiley and Sons Inc., 1989, pp. 103-128.
- [25] IAEA, "Reactor Protection System," IAWA, 2021. [Online]. Available: [https://ansn.iaea.org/Common/documents/Training/TRIGA%20Reactors%20\(Safety%20and%20Technology\)/chapter3/mainsystem52.htm](https://ansn.iaea.org/Common/documents/Training/TRIGA%20Reactors%20(Safety%20and%20Technology)/chapter3/mainsystem52.htm). [Accessed 31 December 2021].

- [26] G. Knoll, "Chapter 14 Slow Neutron Detection Methods," in *Radiation Detection and Measurement, 2nd ed*, United States, John Wiley and Sons Inc., 1989, pp. 481-493.
- [27] T. Hilden, "A gaseous proportional counter built from a conventional aluminum beverage can," *American Journal of Physics*, vol. 83, no. 8, p. 2, 2013.
- [28] N. O. Boyce, "Thermal Neutron Point Source Imaging using a Rotating Modulation Collimator (RMC)," SEMANTIC SCHOLAR, 2010.
- [29] G. Knoll, "Chapter 15 Fast Neutron Detection and Spectroscopy," in *Radiation Detection and measurement, 2nd*, United States, John Wiley and Sons Inc., 1989, pp. 514-549.
- [30] R. H. Olsher, H.-H. Hsu, A. Beverding, J. H. Kleck, W. H. Casson, D. G. Vasilik and R. T. Devine, "WENDI AN IMPROVED NEUTRON REM METER.," *Health Physics*, vol. 79, no. 2, pp. 170-181, 2000.
- [31] JANIS Web, "Incident neutron data / ENDF / B-VII.1 / He3 / MT = 103 : (z,p) / Cross Section," JANIS Web, 2022. [Online]. Available: <https://www.oecd-neo.org/janisweb/renderer/640>. [Accessed 4 January 2022].
- [32] JANIS Web, "Incident Neutron Data/ENDF/B-VII.1/Cl35/MT=103: (z,p)/Cross section," JANIS Web, 2022. [Online]. Available: <https://www.oecd-neo.org/janisweb/renderer/650>. [Accessed 4 January 2022].
- [33] R. Machrafi, A. Miller and Khan N., "New approach to neutron spectrometry with multi element scintillator," *Radiation Measurement*, vol. 80, no. ELSEVIR Ltd., pp. 10-16, 2015.

- [34] Shalom EO, "LaCl₃(Ce) Scintillator Crystals," Shalom EO, 2022. [Online]. Available: [https://www.shalomeo.com/Scintillators/LaCl₃-Ce/product-396.html](https://www.shalomeo.com/Scintillators/LaCl3-Ce/product-396.html). [Accessed 8 January 2022].
- [35] Jagdish K. Tuli et al., "Nuclear Data Sheets," National Nuclear Data Center, [Online]. Available: <https://www.nndc.bnl.gov/nds/>. [Accessed 10 January 2022].
- [36] N. Khan, "A New Approach to Neutron Spectrometry with Multi-Element Scintillators," Ontario Tech University, Oshawa, 2014.
- [37] Los Alamos National Laboratory, "Monte Carlo Methods, Codes, & Applications Group," Los Alamos National Laboratory, [Online]. Available: <https://mcnp.lanl.gov/>. [Accessed 2 February 2022].
- [38] S. M. Malkapur and M. C. Narasimhan, "Virgin and waste polymer incorporated concrete mixes for enhanced neutron radiation shielding characteristics," in *Use of Recycled Plastics in Eco-efficient Concrete*, Woodhead Publishing, 2019, pp. 215-247.
- [39] A. Hossain, M. Rahman and M. Kamal, "Assessment of Terrestrial Radionuclides in the Northern part of Chittagong City Corporation, Chittagong, Bangladesh," Research Gate, 2019.
- [40] T. Piotrowski, D. Tefelski, A. Polanski and J. Skubalski, "Monte Carlo simulations for optimization of neutron shielding concrete," *Central European Journal of Engineering*, vol. 2, no. 2, pp. 296-303, 2012.

APPENDIXES

Appendix A – Materials Tables in MCNP/X

Table A.0.1: Material Input for Lathanum Choride

Material	Density (g/cm ³)	Element	Cross-section Library	Weight Fraction (%)
Lathanum Choride (LaCl ₃)	3.85	La	57139.70c	17.8
		Cl	17035.70c	0.822

Table A.0.2: Material Input for Air

Material	Density (g/cm ³)	Element	Cross-section Library	Weight Fraction (%)
Air	1.225*10 ⁻³	N	7014.70c	78
		O	8016.70c	22

Table A.0.3: Material Input for Heavy Concrete[40]

Material	Density (g/cm ³)	Element	Cross-section Library	Weight Fraction (%)
Heavy Concrete	3.8	H	1001.70c	0.62
		C	6000.70c	0.04
		O	8016.70c	31.65
		Na	11023.70c	0.03
		Mg	12024.70c	0.12
		Al	13027.70c	0.69
		Si	14028.70c	2.95
		S	16032.70c	10.63
		Cl	17035.70c	0.02
		K	19039.70c	0.13
		Ca	20040.70c	3.89
		Fe	26056.70c	4.11
Ba	56137.70c	45.12		

A.1 sub-Appendix

40. Piotrowski, T., et al., *Monte Carlo simulations for optimization of neutron shielding concrete*. Central European Journal of Engineering, 2012. **2**(2): p. 296-303.

Appendix B – MCNP/X Code for ²²Na Gamma Detection

```

c====Block 1: Cells Cards====
c  LaCl Cylinder cell
  40  1 -3.85  -3  IMP:P=1
c  Space in the Bunker air
  41  2 -1.225E-3 3 3 -2 IMP:P=1
c  Space outside the Bunker void
  42  0      1  IMP:P=0
c  Heavy Concrete side walls
  43  2 -1.225E-3 -1 2  IMP:P=1

c====Block 2: Surface Cards====
c  Rectangular Room Outside
  1  RPP -757.5 477.5 -477.5 477.5 -185 315
c  Rectangular Room Inside
  2  RPP -677.5 377.5 -377.5 377.5 -85 215
c  Cylinder LaCl3
  3  RCC 0 -11.905 -1.905 0 0 -3.81 1.905
c

c====Material Cards====
c -----LaCl-----
m1  57139.70c -0.178
    17035.70c -0.822
c -----Air-----
m2  7014.70c -0.78
    8016.70c -0.22
c====Block 3 Data Cards====
mode P
PHYS:P 100 0 0 0 0
SDEF PAR = 2 ERG = d1 POS = 0 -11.905 -
1.905
--Removed intentionally--
ctme 120
F8:P
FT8 GEB --Removed intentionally--
c -----Energy Bining for Tally 8-----
E8  0.00 &
    0.01 &
    0.02 &
    ...
    6.00

```

Appendix C – MCNP/X Code for ^{35}Cl (n, p) ^{35}S Reaction

```

c ===Block 1: Cells Cards===
m2 7014.70c -0.78 $MAT2
c Lacl Cylinder cell
8016.70c -0.22
40 1 -3.85 -3
c -----Heavy Concrete-----
c Space in the Bunker air
m3 1001.70c -0.0062
41 2 -1.225E-3 3 -2
6000.70c -0.0004
c Space outside the Bunker void
8016.70c -0.3165
42 0 1
11023.70c -0.0003
c Heavy Concrete side walls
12024.70c -0.0012
43 3 -3.8 -1 2
13027.70c -0.0069
c ===Block 2: Surface Cards===
14028.70c -0.0295
c Rectangular Room Outside
16032.70c -0.1063
1 rpp -757.5 477.5 -477.5 477.5 -185 315
17035.70c -0.0002
c Rectangular Room Inside
19039.70c -0.0013
2 rpp -677.5 377.5 -377.5 377.5 -85 215
20040.70c -0.0389
c Cylinder LaCl3
26056.70c -0.0411
3 rcc 0 -11.905 -1.905 0 0 -3.81 1.905
56137.70c -0.4512
c ===Block 3 Data Cards===
imp:n 1 1r 0 1 $ 40, 43
mode n h
imp:h 1 1r 0 1 $ 40, 43
c
phys:n 100 2.5 0 -1
c ===Material Cards===
sdef PAR = N ERG = 2.5 POS = 0 -11.905
12.095
c -----LaCl-----
--Removed intentionally--
m1 57139.70c -0.178 $MAT1
f8:h
17035.70c -0.822
f8 GEB --Removed intentionally--
c -----Air-----

```

c -----Energy Bining for Tally 8-----	0.02 &
e8 0.00 &	...
0.01 &	6.00

Appendix D – MCNP/X Code for $^{35}\text{Cl} (n, \alpha) ^{32}\text{P}$ Reaction

```

c ===Block 1: Cells Cards===
c -----Air-----
c Lacl Cylinder cell
40 1 -3.85 -3 IMP:N,A=1
8016.70c -0.22
c Space in the Bunker air
c -----Heavy Concrete-----
41 2 -1.225E-3 3 -2 IMP:N,A=1
m3 1001.70c -0.0062
6000.70c -0.0004
c Space outside the Bunker void
42 0 1 IMP:N,A=0
8016.70c -0.3165
c Heavy Concrete side walls
11023.70c -0.0003
43 3 -3.8 -1 2 IMP:N,A=1
12024.70c -0.0012
13027.70c -0.0069
c ===Block 2: Surface Cards===
c Rectangular Room Outside
1 RPP -757.5 477.5 -477.5 477.5 -185
315
16032.70c -0.1063
17035.70c -0.0002
c Rectangular Room Inside
2 RPP -677.5 377.5 -377.5 377.5 -85
215
19039.70c -0.0013
20040.70c -0.0389
c Cylinder LaCl3
26056.70c -0.0411
3 RCC 0 -11.905 -1.905 0 0 -3.81
1.905
56137.70c -0.4512
c ===Block 3 Data Cards===
mode N A
c
PHYS:N 100 2.5 0 -1
c ===Material Cards===
SDEF PAR = N ERG = 2.5 POS = 0 -11.905
c -----LaCl-----
12.095
m1 57139.70c -0.178
--Removed intentionally--
17035.70c -0.822
F8:A

```

FT8 GEB --Removed intentionally— 0.02 &
c -----Energy Bining for Tally 8-----
E8 0.00 & ...
0.01 & 6.00

Appendix E – MCNP/X Code for ³⁵Cl (n, γ) Reaction

```

c ===Block 1: Cells Cards===
m1 57139.70c -0.178 $MAT1
c Lacl Cylinder cell
17035.70c -0.822
40 1 -3.85 -3
c -----Air-----
c Space in the Bunker air
m2 7014.70c -0.78 $MAT2
41 2 -1.225E-3 3 -2
8016.70c -0.22
c Space outside the Bunker void
c -----Heavy Concrete-----
42 0 1
m3 1001.70c -0.0062
c Heavy Concrete side walls
6000.70c -0.0004
43 3 -3.8 -1 2
8016.70c -0.3165
11023.70c -0.0003
c ===Block 2: Surface Cards===
12024.70c -0.0012
c Rectangular Room Outside
13027.70c -0.0069
1 1 rpp -757.5 477.5 -477.5 477.5 -185
14028.70c -0.0295
315
16032.70c -0.1063
c Rectangular Room Inside
17035.70c -0.0002
2 1 rpp -677.5 377.5 -377.5 377.5 -85 215
19039.70c -0.0013
c Cylinder LaCl3
20040.70c -0.0389
3 1 rcc 0 -11.905 -1.905 0 0 -3.81 1.905
26056.70c -0.0411
56137.70c -0.4512
c ===Block 3 Data Cards===
imp:n 1 1r 0 1 $ 40, 43
mode n p
imp:p 1 1r 0 1 $ 40, 43
c
phys:n 100 2.5 0 -1
c ===Material Cards===
sdef PAR = N ERG = 2.5 POS = 0 -11.905
c -----LaCl-----
12.095

```

--Removed intentionally—	0.01 &
f8:p	0.02 &
ft8 GEB --Removed intentionally—	...
c -----Energy Bining for Tally 8-----	6.0
e8 0.00 &	